

# In-situ observation of powder spreading in powder bed fusion metal additive manufacturing process using particle image velocimetry

Seungkyun Yim<sup>a,b,\*</sup>, Jiayu Sun<sup>a</sup>, Koki Minowa<sup>c</sup>, Hao Wang<sup>a,b</sup>, Kenta Aoyagi<sup>a,\*\*</sup>, Kenta Yamanaka<sup>a</sup>, Akihiko Chiba<sup>a,b</sup>

<sup>a</sup> Institute for Materials Research, Tohoku University, 2-1-1 Katahira, Sendai, Miyagi 980-8577, Japan

<sup>b</sup> New Industry Creation Hatchery Center (NICHe), Tohoku University, 2-1-1 Katahira, Sendai, Miyagi 980-8577, Japan

<sup>c</sup> Department of Materials Processing, Tohoku University, 6-6-02 Aobayama, Sendai, Miyagi 980-8579, Japan

## ARTICLE INFO

### Keywords:

Powder bed fusion additive manufacturing  
Powder spreading mechanism  
Particle image velocimetry  
Discrete element method  
In-situ observation

## ABSTRACT

Providing a dense powder bed is necessary to ensure the rationality of the final product prepared by powder bed fusion-based additive manufacturing under broad building parameters. In this study, the powder spreading mechanism was elucidated using particle image velocimetry and discrete element simulations. The particle flow regimes in the spreading process were identified based on the particle displacement: alignment, rotation, and deposition. The alignment regime was dominant in gas-atomized stainless steel 304 powder piles, whereas the rotation regime was dominant in plasma rotating electrode processed stainless steel 304 powder piles. A high-fidelity spreading simulation model was developed to clarify the critical factors resulting in the different flow regimes of different stainless steel 304 powders. The dominant rotational regime of the plasma rotating electrode processed powder was substituted for alignment by increasing the cohesive force. The particle supply in the spreading process was further suppressed by increasing the cohesive force, owing to the formation of a strong force arch and agglomeration. The high cohesive force in the gas-atomized powder was mainly attributed to the electrostatic force caused by the thick oxide film. Therefore, it was proven that the oxide film thickness is a key factor in determining the powder spreading mechanism and powder bed quality in the powder bed fusion additive manufacturing process.

## 1. Introduction

In recent decades, metal additive manufacturing (AM) techniques have received significant attention in the aerospace and automobile industries for fabrication of complex and lightweight structural components [1]. In particular, powder bed fusion-based additive manufacturing (PBF-AM) techniques, such as laser powder bed fusion (L-PBF) and electron beam powder bed fusion (EB-PBF), have been actively researched and developed because of their many advantages, including good surface finish, structural design accuracy, and superior mechanical properties [2,3]. The general principle of the PBF-AM technique is that a thin powder layer is first spread on a building plate and then melted using a high-energy beam source in a layer-upon-layer fashion [4]. Thus, the quality of the as-built part produced via PBF-AM is affected by several variables such as the beam intensity, scan speed, line order strategy, preheating temperature, and powder bed properties

including size distribution, shape, and surface conditions [5–7].

Several studies have reported tailored microstructures that satisfy the desirable mechanical properties of structural materials using PBF-AM techniques. Zelaia et al. fabricated a single-crystal Ni-based superalloy using EB-PBF [8]. Wang et al. fabricated single-crystal austenitic stainless steel with superior ductility using L-PBF technology [9]. Lei et al. demonstrated site-specific control of solidified grains in the EB-PBF process; however, it required strict process parameter optimization [10, 11]. Besides, many studies have been conducted to reduce internal defects in as-built parts produced by the PBF-AM technique. Aoyagi et al. reported that the internal microdefects of an as-built part can be reduced by process parameter optimization using a support vector machine; however, high-quality products are only obtained under a restricted parameter set [12,13]. Rausch et al. reported that internal defects in the as-built part were suppressed by increasing the powder bed quality during the PBF-AM process [14]. Zhao et al. demonstrated that the

\* Corresponding author at: Institute for Materials Research, Tohoku University, 2-1-1 Katahira, Sendai, Miyagi 980-8577, Japan.

\*\* Corresponding author.

E-mail addresses: [yim.seungkyun.a3@tohoku.ac.jp](mailto:yim.seungkyun.a3@tohoku.ac.jp) (S. Yim), [kenta.aoyagi.e7@tohoku.ac.jp](mailto:kenta.aoyagi.e7@tohoku.ac.jp) (K. Aoyagi).

**Table 1**

Alloy composition of SUS304 powders produced by gas atomization and plasma rotating electrode process.

Sample	Alloy composition (wt%)						
	Fe	Cr	Ni	Mn	Si	C	P
GA SUS304	70.53	18.67	9.02	1.04	0.66	0.06	0.02
PREP SUS304	69.61	19.31	9.87	0.83	0.34	0.03	0.01

internal defects of the final product in the EB-PBF process can be restricted under broad process parameters by optimizing the powder bed quality [15]. Therefore, providing a high-quality powder bed is a prerequisite for attaining tailored microstructures without internal defects in as-built products produced via PBF-AM.

Some experimental studies have focused on the characteristics of the powder feedstock to optimize the powder bed quality during the spreading process. Snow et al. suggested that the spreadability and paving density of a powder are proportional to its flowability [16]. Nan et al. reported that the packing density of the powder bed increased with decreasing flowability owing to the suppressed particle motion [17]. Mussatto et al. pointed out that the quality of the powder bed was dominated by the particle morphology rather than the flowability [18]. Yim et al. reported that the superior spreadability and packing quality of the powder were mainly attributed to cohesive forces during the spreading process [19]. Despite numerous experimental studies on powder spreading, the key factor determining the powder packing quality has been controversial owing to the unclear spreading mechanism. Furthermore, in situ observation of powder spreading is challenging owing to observation difficulties such as the discrete nature, particle overlapping, micro-time scale, and limited resolution [20]. Escano et al. suggested high-speed X-ray imaging for the in situ observation of powder spreading, but they only focused on the slope analysis of the powder pile owing to particle overlapping at the center region [21,22]. As an alternative route to in situ observation, many studies have been conducted to improve the powder bed quality in the PBF-AM

process using discrete element method (DEM) simulations [23–28]. However, the particle flow behavior in the DEM simulation is significantly dependent on simulation parameters, such as friction, damping, and cohesion coefficients [29]. Therefore, a new strategy for the in situ observation of powder spreading should be developed to clarify the spreading mechanism and accurately calibrate the simulation parameters.

The aim of this study was to elucidate the powder-spreading mechanisms using coupled in situ observations and DEM simulations. A novel in situ observation system for powder spreading is developed using particle image velocimetry (PIV). The spreading mechanisms were evaluated using two different powder feedstocks produced via gas atomization (GA) and plasma rotating electrode process (PREP). The factors determining the spreading behavior and powder bed quality were investigated using four virtual powders produced by the high-fidelity DEM simulation. Finally, the key factor causing the cohesive force in the GA powder is discussed using electrical resistance test results. We believe that our study offers an alternative strategy for the in situ observation of powder spreading and can contribute to the optimization of the PBF-AM process.

## 2. Materials and methods

### 2.1. Particle size and shape characterization

Stainless steel 304 (SUS304) powders produced by gas atomization and the plasma rotating electrode process were prepared by the Japan Additive Manufacturing & Processing Technology Corp. (JAMPT, Japan). The alloy compositions of the powders were analyzed using inductively coupled plasma mass spectrometry (ICP-OES, Spectro Arcos Analytical Instruments, Germany), and their chemical composition was similar (Table 1). The particle size distribution of the powders was determined using a laser diffraction particle size analyzer (MT3000II, Microtrac Retsch GmbH, Germany). The particle morphologies of the powders were characterized by scanning electron microscopy (SEM, S-

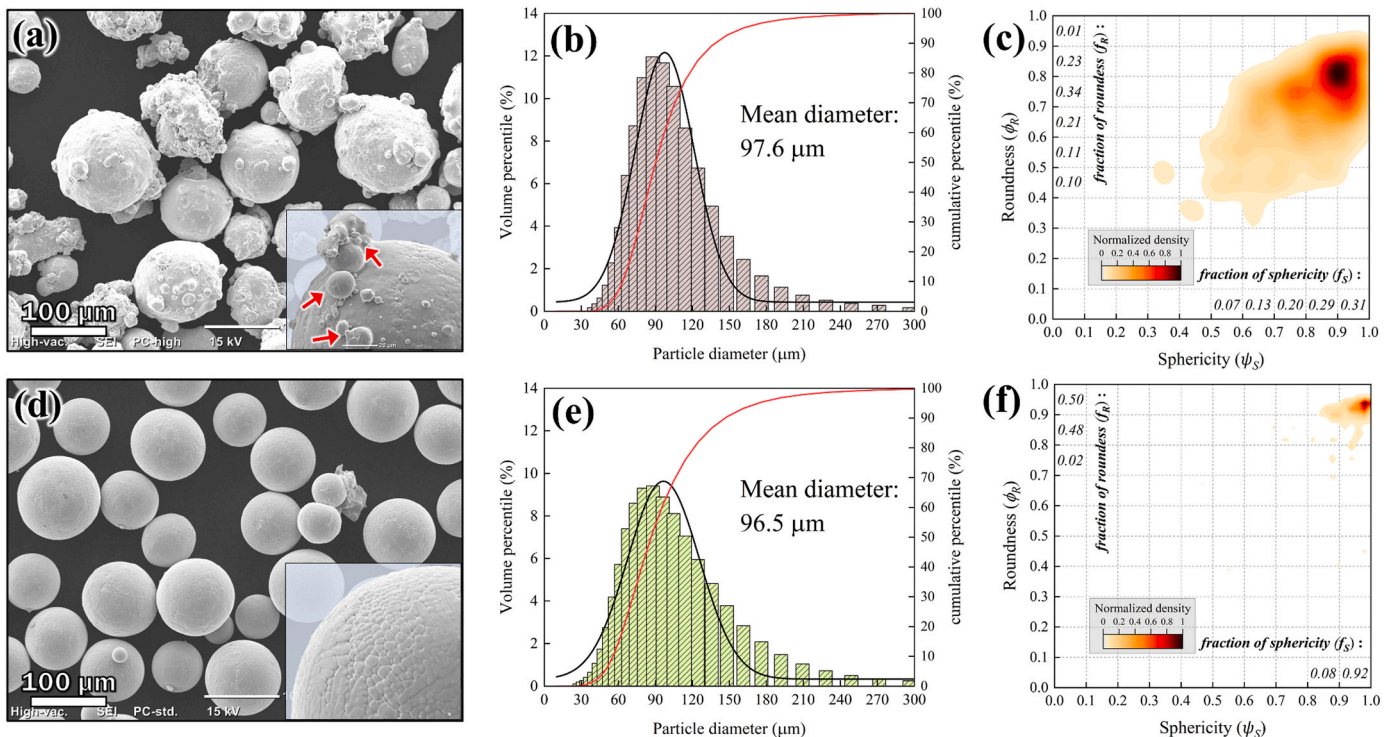


**Fig. 1.** (a), (d) Particle morphology images with magnified surface, (b), (e) particle size distribution, (c), (f) particle morphology density map. (a), (b), (c) GA SUS304 powder, (d), (e), (f) PREP SUS304 powder. (Red arrow indicates surface attached satellites).

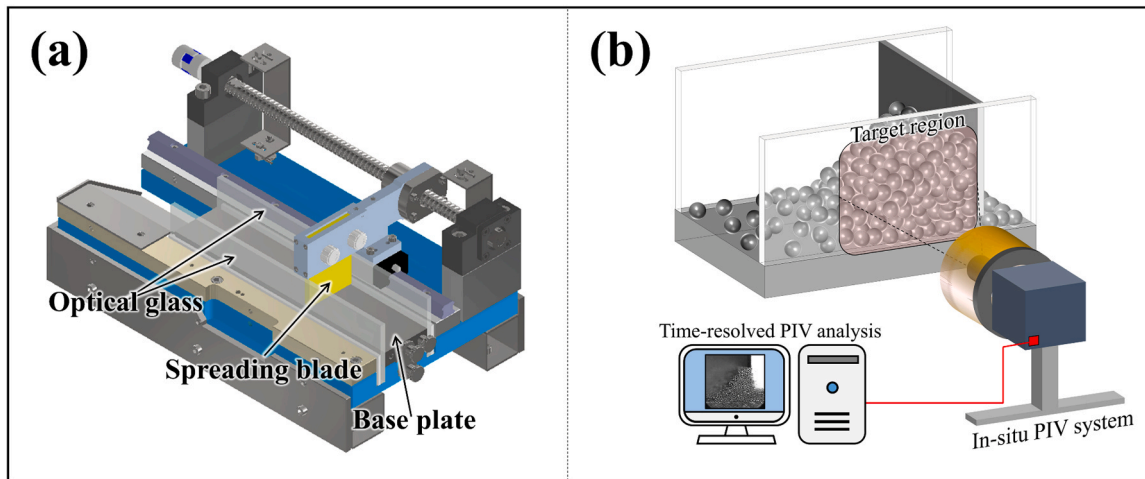


Fig. 2. Schematics of powder spreading equipment and developed particle image velocimetry system for in-situ observation.

3400N, Hitachi High-Tech Science Corp., Japan). Particle morphology analysis was performed to classify the regularity of the particle shape using ImageJ software (National Institutes of Health, USA). The sphericity ( $\psi_S$ ) and roundness ( $\phi_R$ ) was determined using > 1000 particles as follows [27]:

$$\psi_S = \left( \frac{r_{a,i}}{r_{m,i}} \right)^2, \quad (1)$$

$$\phi_R = \left( \frac{r_{a,i}}{r_{p,i}} \right)^2, \quad (2)$$

where  $r_{a,i}$ ,  $r_{m,i}$ , and  $r_{p,i}$  denote the computed radii based on the area, major axis, and perimeter of particle  $i$ . Therefore, the  $\psi_S = 1$  indicates the spherical shape without elongation on the shape, and the  $\phi_R = 1$  indicates the smooth surface without irregular fluctuations [27]. A particle morphology density (PMD) map was constructed to examine the particle shape distributions in the GA and PREP powders. Multivariate kernel density estimation was performed to visualize the probability density of the particle shape using Originpro2022 software (OriginLab Corp., USA). The elongated particles in the PMD map were defined as those with  $\psi_S < 0.9$ . The particle surface images of the GA and PREP powders are presented in Fig. 1a and d. The GA powder consists of spherical and elongated particles with many satellites, whereas the PREP powder consists of almost spherical particles with smooth surfaces. The particle size distribution of GA and PREP powders ranged from 25 to 180  $\mu\text{m}$  to minimize the particle agglomeration by van der Waals force in the spreading process [23]. In the PMD map, the elongated particle fraction of GA powder was examined to be 0.69, while that of PREP was to be 0.08 (Fig. 1c and f). The  $\phi_R$  of GA powder ranged from 0.4 to 1.0 indicating irregular particle surface owing to the united satellites on the surface, while that of PREP powder was above 0.7 representing good surface finishing.

## 2.2. Electrical properties and oxide film characterization

The electrical properties of powders were examined to estimate the electrostatic force caused by triboelectric charge in the powder spreading process. The direct current (DC) electrical resistivity was determined via four-point probe measurements using powdered samples. The powder (5 g) was placed inside a measuring  $\text{Al}_2\text{O}_3$  cylinder and pressed by 10 N electrodes under vacuum. Impedance spectroscopy measurements with alternating current (AC) were performed to investigate the electrical properties such as the resistance, capacitance, and inductance of the powders. The impedance data were recorded in the frequency range of  $1\text{--}2 \times 10^6$  Hz using an LCR meter (ZM 2376 LCR, NF

Corp., Japan). The composition and thickness of the oxide films were examined using X-ray photoelectron spectroscopy (XPS; PHI5000 VersaProbe II, ULVAC-PHI Inc., Japan). The survey spectra were collected to identify major chemical elements of oxide film using a monochromatic  $\text{Al K}\alpha$  source. Depth profiling was performed using an  $\text{Ar}^+$  ion beam with kinetic energy of 1 keV to determine the oxide film thickness. An etching rate of 7.57 nm/min calibrated using a  $\text{SiO}_2$  standard, was used. The surface atomic concentration was analyzed using a Common Data Processing System (version 12) with a Shirley background correction [30].

## 2.3. Powder spreading experiment

The powder spreading experiment was performed using in-house powder spreading equipment (Fig. 2a). Both sides of the base plate were sealed using flexible glass to observe microscale particle dynamics during the spreading process. The height of the stainless-steel blade was carefully calibrated using a height standard specimen with a thickness of 300  $\mu\text{m}$ , which is the effective layer thickness of the PBF-AM process [31]. The powder (20 g) was inserted in front of the spreading blade using a hole flow supplier, and powder spreading was conducted at a velocity of 50 mm/s using the GA and PREP powders. In-situ observations of powder spreading were conducted using a specially designed particle image velocimetry system (Fig. 2b). PIV is a type of Time of Flight measurement technique that effectively calculates the velocity and displacement of a given fluid within a target observation region [32]. A high-speed camera (Phantom T4040, Vision Research Inc., USA) with multiple light-emitting diode systems was used to examine particle movement on a microsecond scale. A high-focal-resolution lens with an insert light was employed to observe the microscale dynamics of the powder-spreading process. The recorded high-resolution images were divided into  $1024 \times 1024$  pixels and the interrogation window area was selected to calculate the particle velocity and displacement at each time step. Standard FFT cross-correlation was employed to obtain the correlation plane for each interrogation window using Koncerto II software (Seika Digital Image Corp., Japan). The displacement and velocity of the particles were calibrated using the peak data detected in each interrogation window. Further detailed algorithms for PIV analysis can be found in a previous study [33]. The packing density ( $\rho_{PB}$ ) was determined from the mass of the powder bed as follows:

$$\rho_{PB} = \frac{m_{PB}}{L \times W \times H} \times \frac{100}{\rho_t}, \text{ b} \quad (3)$$

where  $m_{PB}$ ,  $L$ ,  $W$ , and  $H$  are the mass, length, width, and height of the deposited powder bed, respectively, and  $\rho_t$  is the bulk density of the

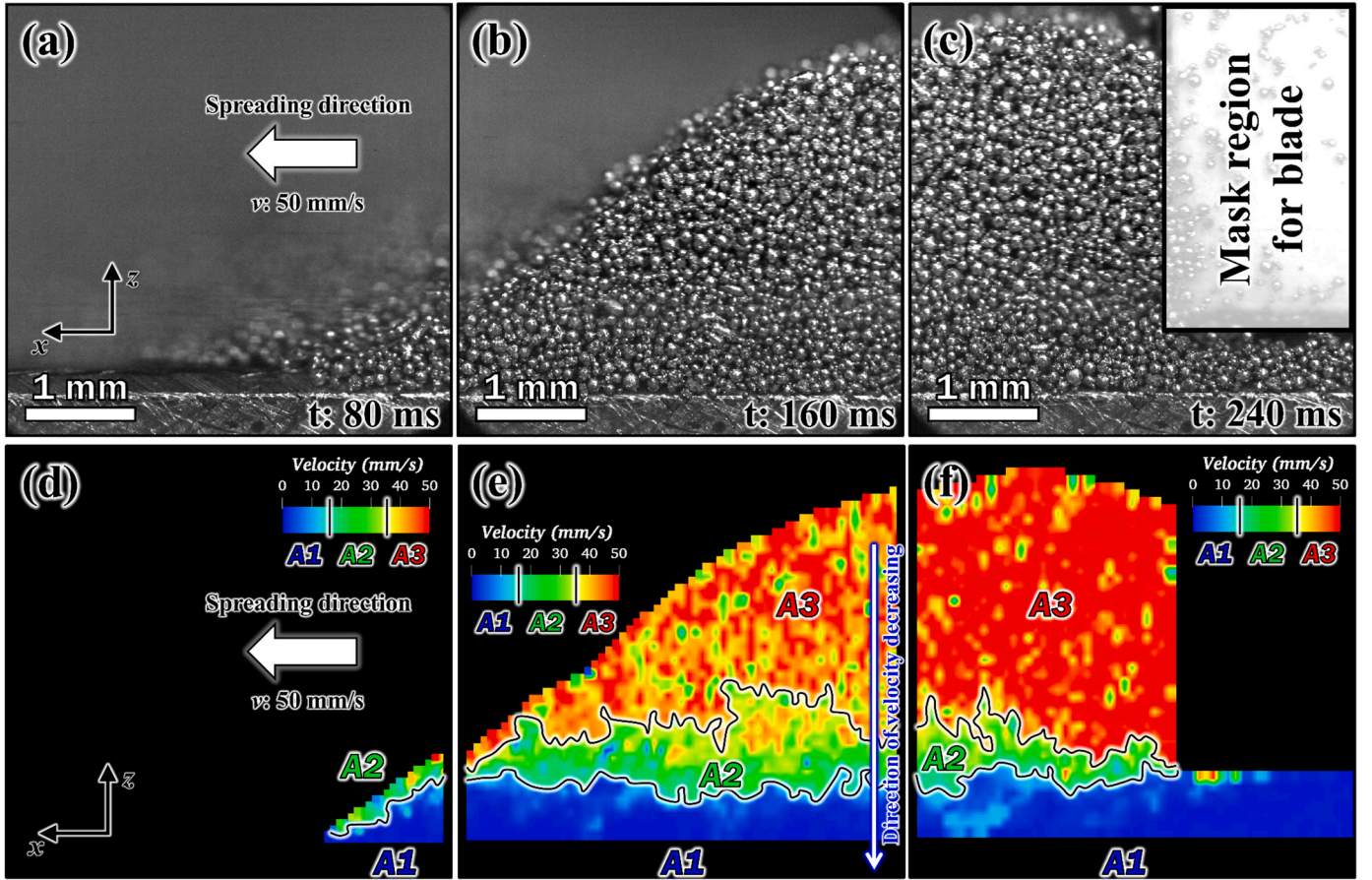


Fig. 3. High-speed camera images of GA powder in the spreading process at a time step; (a) 80 ms, (b) 160 ms, and (c) 240 ms. The calculated velocity distribution via PIV analysis at a time step; (d) 80 ms, (e) 160 ms, and (f) 240 ms. (Blue colored arrow indicates the direction of velocity decreasing in the powder pile).

SUS304 powder ( $7.93 \text{ g/cm}^3$ ). The detailed packing density measurement method can be found in our previous study [19]. The surface topography of the powder bed was examined by stereoscopic imaging with a resolution of  $\pm 2.5 \mu\text{m}$  using a 3D optical profiler system (VR-3200, Keyence Corp., Japan). The surface roughness ( $Sa$ ) of the powder bed was determined as follows:

$$Sa = \frac{1}{K} \iint_K |Z(x, y)| dx dy, \quad (4)$$

where  $K$  is the target area for observation and  $Z$  is the height distribution of each data point in the observation field. Powder-spreading experiments were performed five times to ensure experimental rationality.

#### 2.4. Discrete element method model

A 3d discrete element method (DEM) simulation was developed to examine the key factors determining the spreading behavior and packing quality of the powder during the spreading process. Based on Newtonian's second law, the viscoelastic Hertz-Mindlin contact equation was solved using the open-source framework YADE [34]. The upper limits of the sliding ( $F_S$ ) and rolling ( $F_R$ ) forces in the particles are expressed using the classic Mohr-Coulomb failure criterion as follows [35]:

$$F_S = \chi_S F_N, \quad (5)$$

$$F_R = \chi_R F_N E_R \omega_p d_p, \quad (6)$$

where  $F_N$  is the normal force applied in the particle,  $\chi_S$  and  $\chi_R$  are the

sliding and rolling friction coefficients, respectively,  $E_R$  is the stiffness in rolling,  $\omega_p$  is the angular velocity, and  $d_p$  is the distance of contact point from the particle center. The viscous damping coefficients limiting the normal ( $\delta_N$ ) and tangential ( $\delta_T$ ) motions can be expressed as follows:

$$\delta_N = \frac{\log e_N}{\sqrt{\pi^2 + (\log e_N)^2}}, \quad (7)$$

$$\delta_T = \frac{\log e_T}{\sqrt{\pi^2 + (\log e_T)^2}}, \quad (8)$$

where  $e_N$  and  $e_T$  denote the restitution coefficients in the normal and tangential directions, respectively. The interparticle friction coefficient comprises the friction and restitution coefficients to simplify the simulation parameter set. In the powder-spreading process, the cohesion or adhesion between metallic particles can be affected by various interactions caused by capillary, electromagnetic, van der Waals, and electrostatic forces [36]. The cohesive interaction force ( $F_C$ ) between particles was integrated to reduce the computational cost using the Derjaguin-Müller-Toporov (DMT) equation:

$$F_C = -4\pi d_p \gamma, \quad (9)$$

where  $d_p$  is the overlapping area of the contacted particle and  $\gamma$  is the surface energy coefficient. Thus, the cohesiveness of the powders was primarily determined by the surface energy coefficient in the DEM simulation. The multi-sphere method was performed to express the elongated particle shape based on  $\psi_S$  with an interval of 0.1. The spherical particles merged into a rigid aggregate, and their inertial tensors were integrated into a single particle. Furthermore, the irregular

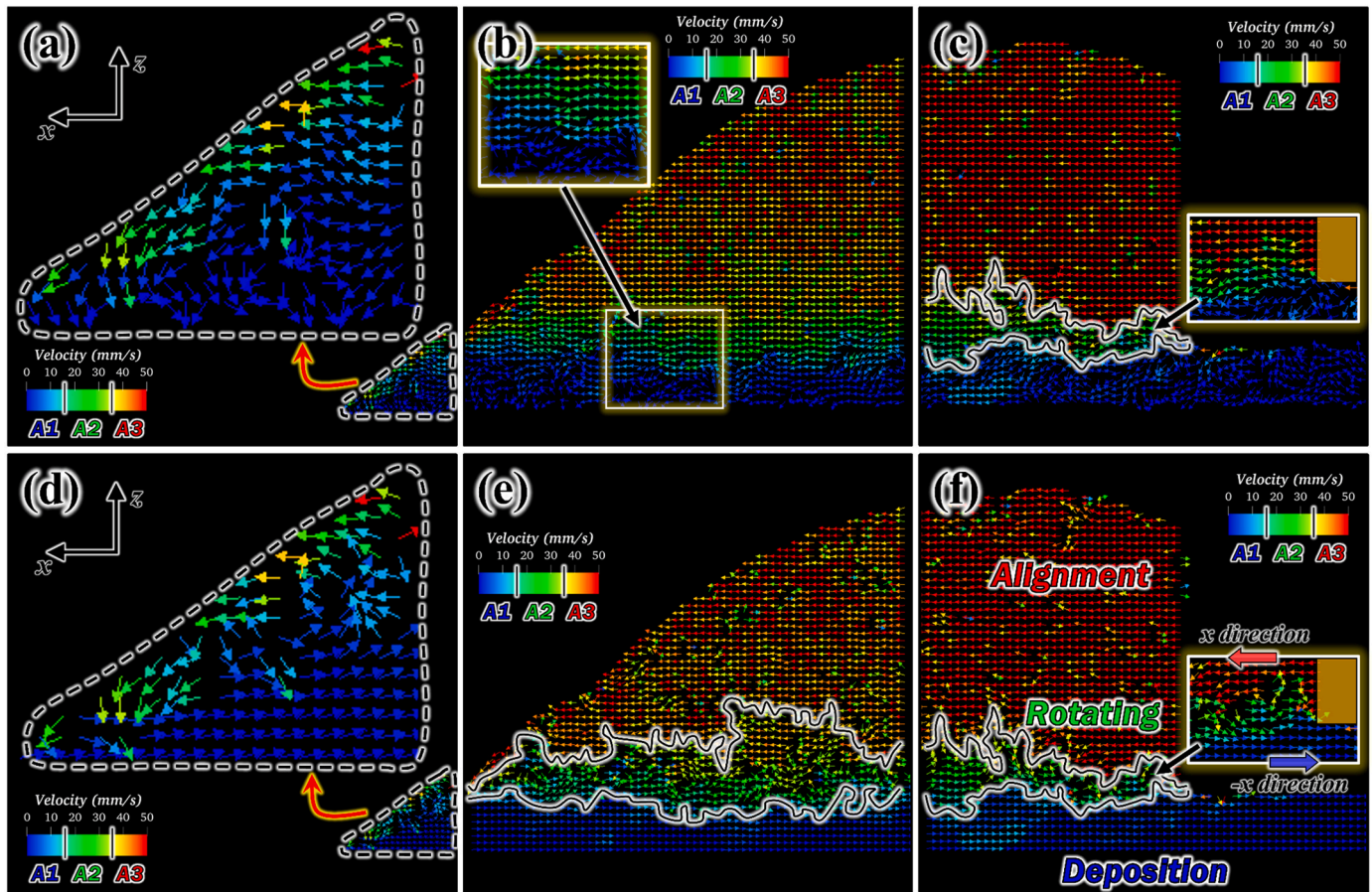


**Fig. 4.** Particle displacements in the GA powder pile obtained by PIV analysis with a time step of; (a) 80 ms, (b) 160 ms, (c) 240 ms; modified particle displacements using fast Lagrangian approaches with a time step of; (d) 80 ms, (e) 160 ms, (f) 240 ms.

particle surface was substituted by interparticle friction in the simulation to enhance the computational efficiency.

### 3. Results and discussion

#### 3.1. In-situ observation of powder spreading mechanism

The in-situ PIV observation was conducted using GA powder under a layer thickness of 300  $\mu\text{m}$  with a spreading velocity of 50 mm/s to clarify the powder spreading mechanism. High-speed camera images of the GA powder pile during the spreading process are shown in Fig. 3a–c. In the in situ PIV observation, the GA powder pile was divided into three parts depending on the time step: front (80 ms), center (160 ms), and end (240 ms). The calculated velocity distribution in the GA powder pile obtained via the PIV analysis is shown in Fig. 3d–f. In the front part, a low-velocity region (denoted as A1) was validated at the bottom site, and an intermediate-velocity (denoted as A2) region was observed at the sloping site (Fig. 3a and d). In the center part of the powder pile, a high-velocity region (denoted as A3) was observed in the upper site owing to the kinetic energy supplied by the spreading blade, whereas the particle velocity decreased to A2 and A1 as decreasing the height in the powder pile (Fig. 3b and e). At the end of the powder pile, the A3 region was identified in the upper site, while the A2 region was observed along the set layer thickness ( $\approx 300 \mu\text{m}$ ) (Fig. 3c and f). This result indicates that the kinetic energy supply in the particles relaxed at a height below the layer thickness and was mainly depleted in the A2 region via multiple interactions with neighboring particles.

The particle displacement in the GA powder pile calculated via PIV analysis is shown in Fig. 4a–c. In the front part, the particle displacement

at the sloping site was aligned in the falling direction, whereas that at the bottom site was randomly distributed because of the dissipated kinetic energy (Fig. 4a). In the center and end parts, the particle displacement at the bottom site showed a random direction with low velocity, whereas that at the upper site was aligned in the  $x$ -direction with high velocity, owing to the residual kinetic energy (Fig. 4b and c). The particle displacement during the spreading process was modified for particle tracking using a fast Lagrangian approach [37]. The mean velocity component in the  $x$ -direction of the particles was extracted from the computational parcel data for tracking the particle displacements. Thus, the modified particle displacement via the fast Lagrangian approach represents the relative angular displacement, which neglects the mean velocity component along the  $x$ -direction during the spreading process. A further detailed algorithm for the fast Lagrangian method can be found in the previous study [38]. The modified particle displacement in the powder pile via the fast Lagrangian approach is shown in Fig. 4d–f. The particle displacement in the A1 region was aligned in the  $-x$  direction, which was the reverse of the blade proceeding direction, indicating powder deposition (Fig. 4d). The particle displacement in A3 region was arrayed along the  $x$ -direction owing to the residual kinetic energy, whereas that in A2 region showed a chaotic distribution (Fig. 4e). In the A2 region, the particles near the bottom and upper sites flowed in reverse, indicating rotation conditions that caused shear stress in the powder pile (Fig. 4f). Thus, the particle flow regimes in the spreading process can be classified based on their displacements such as alignment, rotation, and deposition.

A schematic of powder spreading with a monitoring box for on-site analysis is shown in Fig. 5a. The region of interest (RoI-v) was selected to examine particle velocity and displacement through the gap region

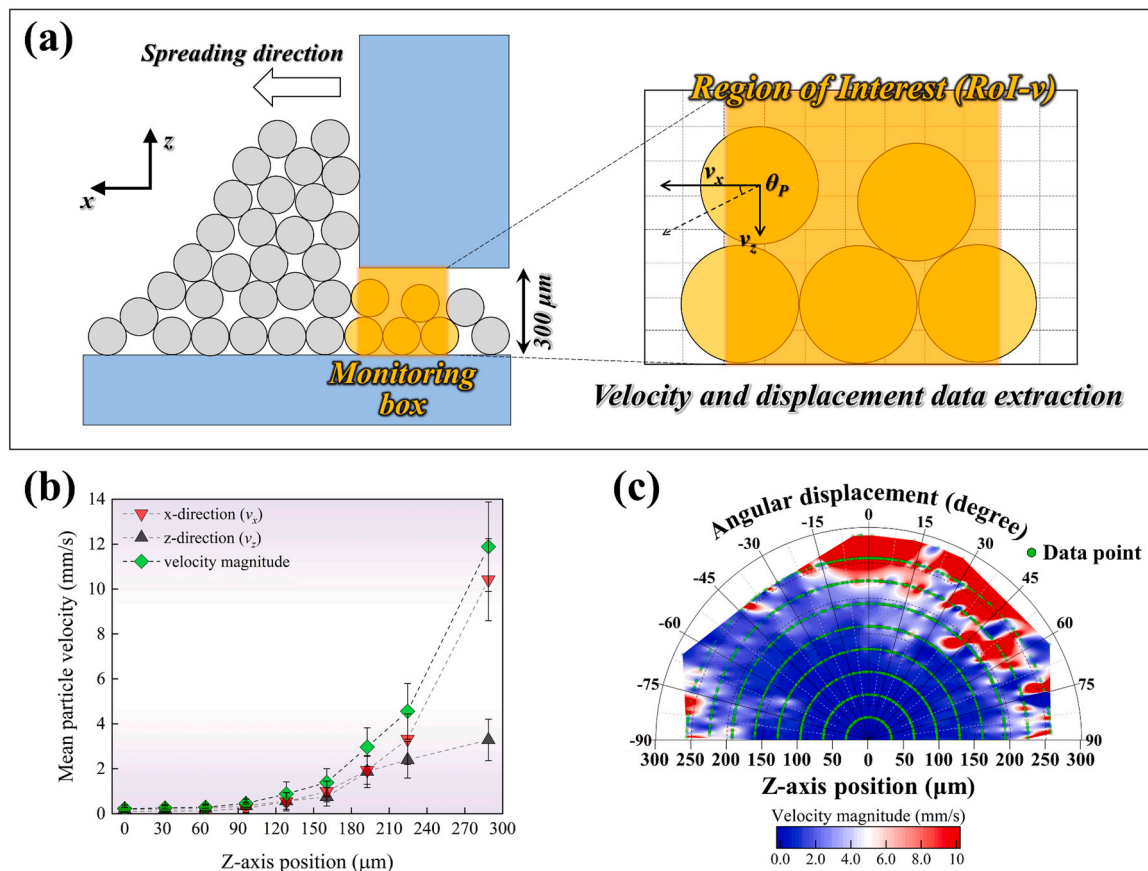


Fig. 5. (a) Schematic of powder spreading with a monitoring box for on-site PIV analysis; (b) average velocity components and (c) angular displacement depending on the z-axis position.

during the spreading process. The linear velocity components in the particles were analyzed using computational parcel data at each time step, and their angular displacement ( $\theta_p$ ) was determined to be  $\arctan(v_z/v_x)$  (Fig. 5a). The average velocity components and angular displacements depending on the z-axis position are shown in Fig. 5b and c. The velocity magnitude of the particles in RoI-v increased with the z-axis position, which was predominantly attributed to the increased velocity along the x-direction (Fig. 5b). The angular displacement of high-velocity particles ranged from  $0^\circ$  to  $60^\circ$  at the z-axis position above  $200 \mu\text{m}$ , while that of low-velocity particles was randomly distributed (Fig. 5c). This result indicates that the kinetic energy in the particles was rapidly dissipated at the bottom region via multiple interactions with neighboring particles or the base plate, resulting in a randomized angular displacement. However, particle movement in the upper region is prolonged after deposition through the gap region owing to residual kinetic energy, resulting in a loosely packed powder bed with surface pores. This result indicates that the powder bed quality in the spreading process is mainly affected by particle interactions in the rotation regime, which causes an irregular particle supply through the gap region.

### 3.2. Influence of powder feedstock on spreading mechanism

The spreading behavior of the GA and PREP powders was investigated using in situ PIV observations to clarify the significance of the powder feedstock on the spreading behavior and powder bed quality. Snapshots of the velocity and modified displacement of the GA and PREP powders are shown in Fig. 6a–l. Three flow regimes of alignment, rotation, and deposition were observed in both the GA and PREP powder piles (Fig. 6d and j), whereas the magnitudes of the A2 region were quite different (Fig. 6a and g). The alignment regime with a high velocity was

dominant in the GA powder pile, whereas the rotation regime with an intermediate velocity prevailed in the PREP powder pile (Fig. 6d and j). A surface plateau was observed in the upper region of the GA powder pile, and the particle displacement was aligned in the x-direction (Fig. 6a and d). By contrast, a smooth surface was observed in the upper region of the PREP powder pile, and its displacement was arrayed in a diagonal direction (Fig. 6g and j). Furthermore, in the upper region, the particles in the GA powder pile move together as agglomerates, whereas those in the PREP powder pile move separately, as shown in appendix video 1. As the spreading blade progressed further, the particles in the GA powder were deposited through the gap region in a parabolic direction at an intermediate velocity (Fig. 6b and e). Freefall particles were observed in front of the blade during the spreading process of the PREP powder and then deposited through the gap region with an intermediate velocity (Fig. 6h and k). The particles of the GA powder pile flowed through the gap region at a low velocity (Fig. 6c and f), whereas those of the PREP powder flowed continuously through the gap region at a high velocity, owing to the high residual kinetic energy (Fig. 6i and l).

Supplementary material related to this article can be found online at [doi:10.1016/j.addma.2023.103823](https://doi.org/10.1016/j.addma.2023.103823).

The monitored velocity components and angular displacements of the GA and PREP powders obtained using RoI-v are shown in Fig. 7a–d. The x-direction velocities of the GA and PREP powders were similar at approximately  $2 \text{ mm/s}$ , whereas the z-direction velocity of the PREP powder was higher than that of the GA powder, owing to the free-falling particles with a high velocity (Fig. 7a and b). The angular displacement of the GA powder was concentrated below  $30^\circ$ , indicating particle flow along the x-direction, and the velocity of most particles was lower than  $4 \text{ mm/s}$  (Fig. 7c). The angular displacement of the PREP powder was homogeneously distributed from  $0^\circ$  to  $90^\circ$ , and the velocity of several

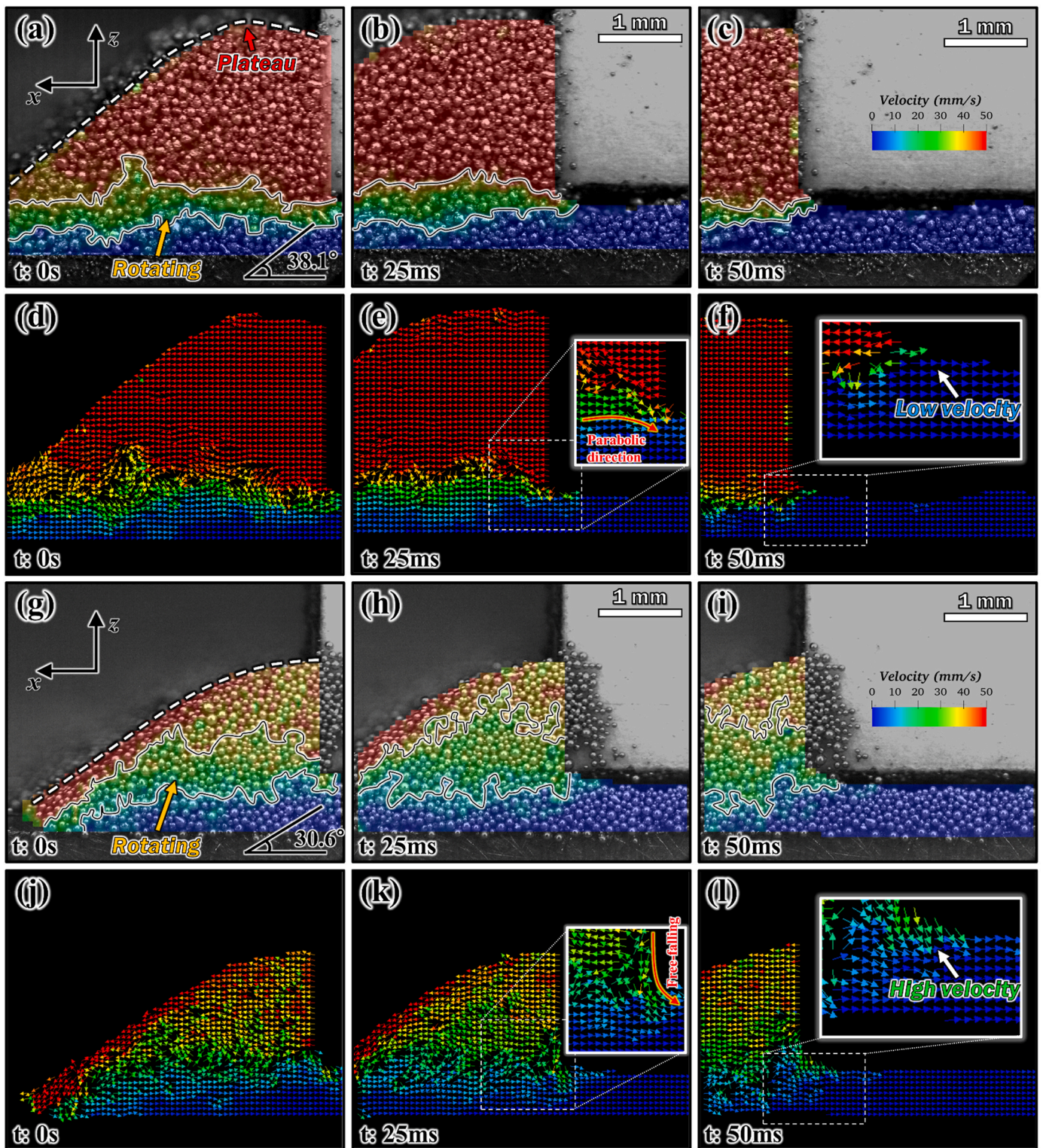
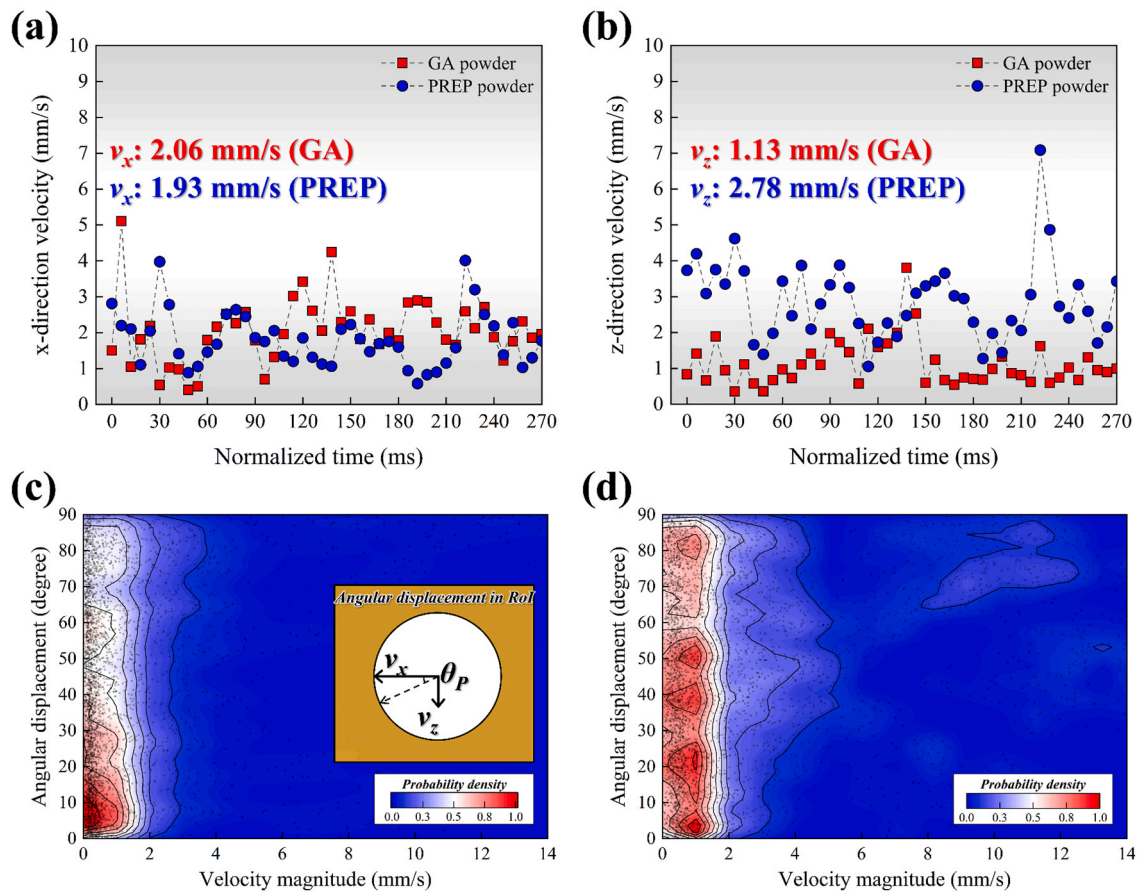


Fig. 6. Snapshot of velocity distribution of GA and PREP powders at a time step of; (a) and (g) 0 s, (b) and (h) 25 ms, (c) and (i) 50 ms; Modified displacement via fast Lagrangian approach in GA and PREP powders at a time step of (d) and (j) 0 s, (e) and (k) 25 ms, (f) and (l) 50 ms.

particles exceeded 8 mm/s (Fig. 7d). As previously mentioned, the alignment regime was predominant in the GA powder pile, and the particles supplied via the gap region were arrayed in a parabolic direction (Fig. 6d–f). Thus, the particles supplied via the gap region could be aligned in the x-direction with a low angular displacement, resulting in a regular particle supply with a low velocity. However, the rotation regime prevailed in the PREP powder pile, and irregular flow was

activated in the powder pile owing to the dominant shear stress. This result suggests that the free-falling particles contribute to the particle supply via the gap region in the PREP powder, which could result in continuous particle flow in the gap region owing to the high residual kinetic energy. Therefore, it was confirmed that the particle deposition behavior of the GA and PREP powders was significantly altered by the different particle flow regimes in the powder pile.



**Fig. 7.** Monitored velocity components of GA and PREP powders obtained in Rol-v; (a) x-direction, (b) z-direction; Monitored angular displacement with velocity; (c) GA powder, (d) PREP powder.

Snapshots of the deposited powder beds and height profiles are presented in Fig. 8a–d. The packing density of the PREP powder bed was determined to be 48.5%, which was superior to that of the GA powder bed (43.8%). The irregular height variation with a high  $Sa$  of  $22.3\ \mu\text{m}$  was obtained in the GA powder bed (Fig. 8c), while the homogeneous height variation with a low  $Sa$  of  $18.1\ \mu\text{m}$  was obtained in the PREP powder bed (Fig. 8d). Interestingly, in the spreading process, the velocity of the PREP powder in the gap region was higher than that of the GA powder owing to the free-falling particles (Fig. 6k). This result indicates that the residual kinetic energy of the particles in the gap region is a minor factor in determining the powder bed quality of PREP powders during the spreading process.

### 3.3. Factor determining the powder bed quality

In the previous section, the powder-spreading mechanism was quite different for the GA and PREP powders despite the same process conditions. A powder-spreading simulation was developed to reveal the critical factors determining the spreading mechanism in GA and PREP powders. A schematic of the powder-spreading model, color-coded by the velocity, is shown in Fig. 9a. The particle displacement obtained from the DEM simulation was converted using the fast Lagrangian method to trace the relative particle trajectories during the spreading process. The particle size distribution of realistic powders was applied to the constructed DEM model. The realistic particles with elongated shapes were implemented using the multi-sphere modeling based on the  $\psi_S$  with the interval of 0.1, as shown in Fig. 9c. The elongated particle fraction ( $f_s$ ), depending on the  $\psi_S$  in the PMD map, was invoked in the DEM model. The interparticle friction and cohesive forces of the GA and

PREP powders were calibrated by fitting the angles of repose under static and dynamic conditions, as shown in Table 2. A more detailed calibration method for the simulation parameters is provided in Appendix 2.

The particle velocities and displacements of the GA and PREP powders in the experiment and DEM simulation are presented in Fig. 10a–h. Three particle flow regimes were identified in the spreading simulations of the GA and PREP powders: alignment, rotation, and deposition, which are in good agreement with the experimental results. In the spreading simulation, the alignment regime with a high velocity was dominant in the GA powder piles, whereas the rotation regime with an intermediate velocity was prevalent in the PREP powder piles. Furthermore, the avalanche angles of the GA and PREP powders in the experiment were in good agreement with those in the DEM simulation. Thus, it can be concluded that the simulation parameters of the GA and PREP powders were well calibrated by comparison with the in situ observation data using the PIV.

The four simulation parameters of the PREP powder were artificially manipulated to clarify the critical factors controlling the spreading mechanism in the PBF-AM process (Fig. 9b). The size distribution, shape distribution, interparticle friction, and cohesive force of the PREP powder were selectively replaced with those of the GA powder, and each virtual powder was referred to as  $P$ -size,  $P$ -shape,  $P$ -friction, and  $P$ -cohesion. The snapshot images of the spreading simulation using the four virtual powders are shown in Fig. 11a–h. The avalanche angle of  $P$ -size powder was confirmed to be  $31.3^\circ$ , which is similar to that of the PREP powder ( $30.9^\circ$ ), as shown in Fig. 11a. The rotation regime was dominant in  $P$ -size powder, and the particle displacement in the alignment region was diagonally arrayed (Fig. 11e), which matched well with the trend of

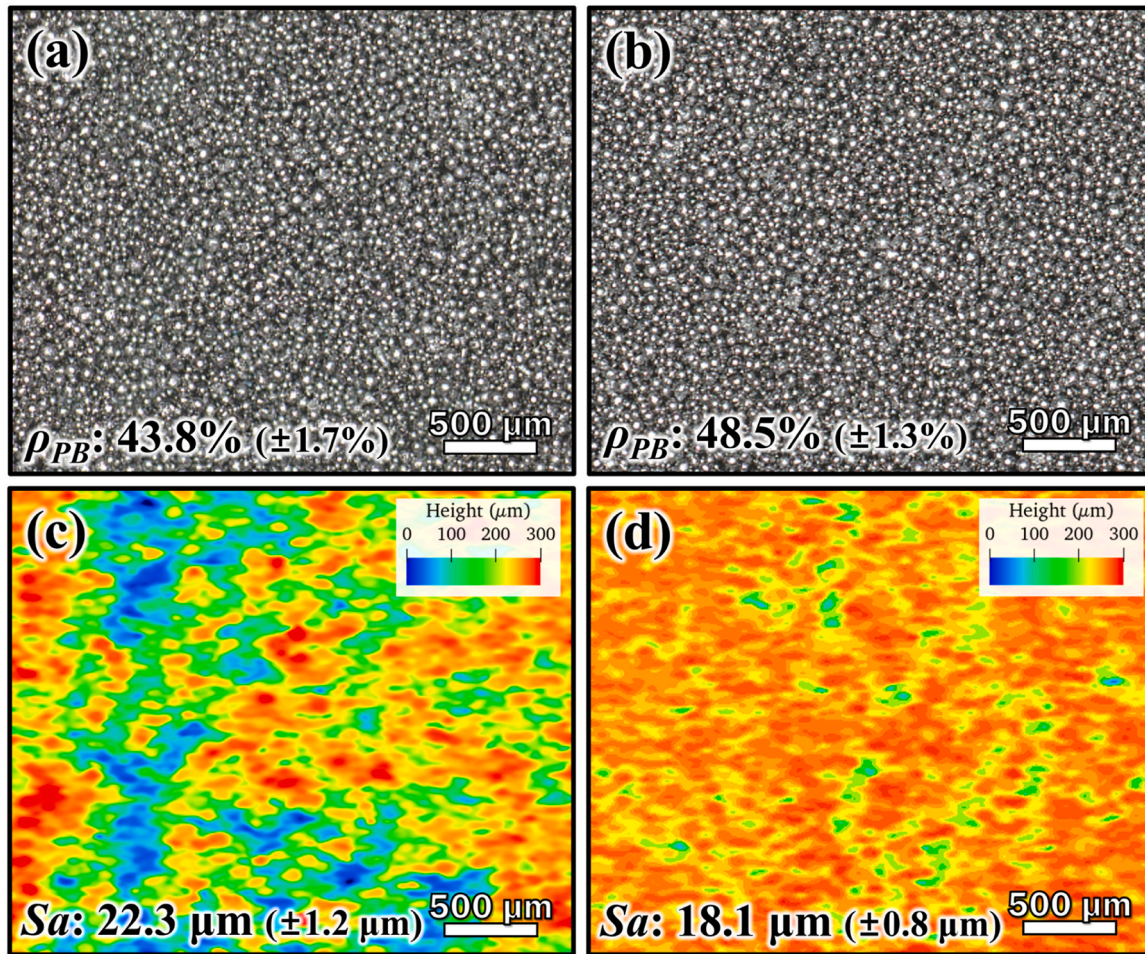


Fig. 8. Snapshot of deposited powder beds; (a) GA powder, (b) PREP powder; corresponding height profiles; (c) GA powder, (d) PREP powder.

the PREP powder (Fig. 10h). This result indicates that the difference in the particle sizes of the GA and PREP powders not contributed to the spreading mechanism. The avalanche angle of *P-shape* powder increased to  $35.2^\circ$  after the addition of nonspherical particles, and a top plateau was observed in the powder pile (Fig. 11b). The rotational regime was dominant in *P-shape* powder, whereas the deposition regime was less dominant (Fig. 11f). Norouzi et al. reported that the flow of elongated particles was limited under rotating conditions because of their arrangement tendency along the preferred orientation [39]. Therefore, the presence of nonspherical particles could result in an increase in the avalanche angle owing to the alignment difficulty of the elongated particles in the dense powder pile [28]. The avalanche angle of *P-friction* powder increased to  $36.3^\circ$  with increasing interparticle friction because of restricted particle sliding and rolling (Fig. 11c). The magnitude of the alignment regime with a high velocity increased, whereas the particle displacement was arrayed in a diagonal direction, representing individual particle movement during the spreading process (Fig. 11g). The highest avalanche angle with a top plateau was obtained for *P-cohesion* powder at  $37.4^\circ$  (Fig. 11d). The alignment regime with high velocity was predominant in the *P-cohesion* powder pile, and the particle displacement was arrayed in the *x*-direction, indicating particle agglomeration (Fig. 11h). Furthermore, the free-falling particles in front of the blade were strongly restricted in *P-cohesion* powder owing to the high cohesive force, which was consistent with the experimental tendency of the GA powder. Thus, it can be deduced that the high avalanche angle of the GA powder originates from the synergetic effects of the addition of nonspherical particles, high interparticle friction, and high cohesive force. In conclusion, the critical factor determining the spreading

mechanism of the GA powder is the cohesive force that causes particle agglomeration.

### 3.4. Elucidation of powder deposition mechanism

The deposited powder beds of the GA and PREP powders in the experiment and DEM simulations are shown in Fig. 12a–f. In the experimental result, the many coarse pores with a size  $> 500 \mu\text{m}$  were observed in the surface of GA powder bed, which resulted in a high *Sa* value of  $22.3 \mu\text{m}$ . (Fig. 12a and b). The surface pore size decreased in the PREP powder bed below  $300 \mu\text{m}$ , and the *Sa* value was reduced to  $18.1 \mu\text{m}$  owing to homogeneous particle deposition (Fig. 12d and e). In the DEM simulation results, the trends of  $\rho_{PB}$  and *Sa* for the GA and PREP powders matched well with the experimental results (Fig. 12c and f).

On-site analysis was performed using a powder-spreading simulation of GA and PREP powders to clarify the powder deposition mechanism. A schematic of powder spreading with on-site analysis boxes is presented in Fig. 13a. The particle flow in *RoI-v* can be affected by the particle interactions in front of the blade owing to the formation of a force arch, which is a strong particle network with an arch shape [28]. Two monitoring regions were delegated to characterize the factors controlling the powder bed quality: *RoI-v* and *RoI-f*. The mass flows, velocity components, and contact forces of the GA and PREP powders during the spreading process are shown in Fig. 13b. The mass flow of GA powder fluctuated below  $9.79 \mu\text{g}$  in the spreading process, and its standard deviation was confirmed to be  $1.73 \mu\text{g}$ . The mass flow of PREP powder was higher than  $12.15 \mu\text{g}$  in the spreading process, and its standard deviation was determined to be  $1.41 \mu\text{g}$ . The mean mass flow of the GA powder

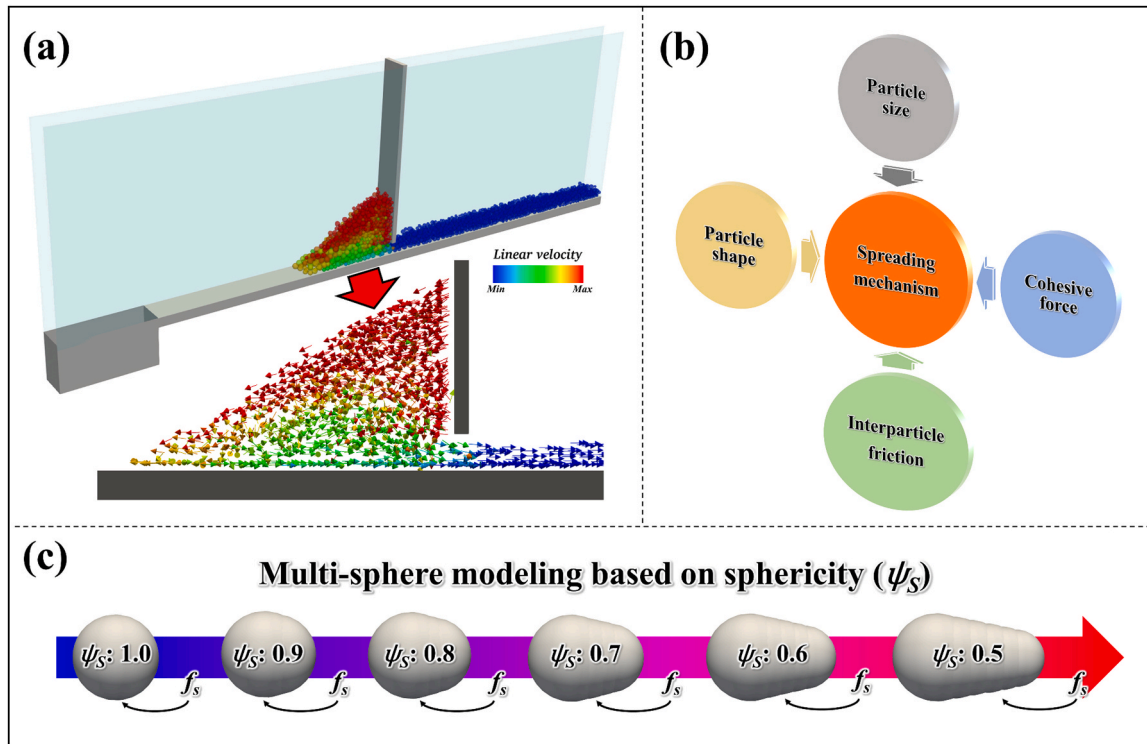


Fig. 9. (a) Schematic of powder spreading model color-coded by velocity, (b) considered DEM simulation parameters for virtual powders, (c) particle model using multi-sphere method.

**Table 2**  
Numerical parameters for DEM simulation.

Parameter	GA powder	PREP powder
Density ( $\rho$ )	7.97 g/cm <sup>3</sup>	
Poisson's ratio ( $\nu$ )	0.265	
Young's modulus ( $E$ )	193 GPa	
Sliding friction coefficient ( $\chi_s$ )	0.43	0.23
Rolling friction coefficient ( $\chi_r$ )	0.36	0.12
Surface energy coefficient ( $\gamma$ )	0.013 J	0.0005 J
Coefficient of restitution between particles ( $e$ )	0.33	0.25
Friction coefficient between particles and optical glass	0.31	0.28
Friction coefficient between particles and stainless steel	0.38	0.31
Numerical damping coefficient	0.02	0.03
Upper limit of time step	3e <sup>-6</sup>	3e <sup>-6</sup>
<b>Material property</b>		
Density of stainless-steel	8.06 g/cm <sup>3</sup>	
Poisson's ratio of stainless steel	0.275	
Young's modulus of stainless steel	203 GPa	
Density of optical glass	1.18 g/cm <sup>3</sup>	
Poisson's ratio of optical glass	0.37	
Young's modulus of optical glass	5.3 GPa	

was examined to be 14.85  $\mu\text{g}$ , which was lower than that of the PREP powder (16.19  $\mu\text{g}$ ). The  $x$ -direction velocity of the PREP powder was similar to that of the GA powder, while the  $z$ -direction velocity was higher owing to the free-falling particles with intermediate velocity, which matched well with the in situ PIV observation results (Fig. 7a and b). This result demonstrates that the residual kinetic energy of the particles in the gap region is a minor factor in determining the packing density during deposition. The average contact force of the GA powder was determined to be 1.48  $\mu\text{N}$ , which was higher than that of the PREP powder (0.76  $\mu\text{N}$ ). However, the mean contact force in  $RoI-f$  was irrational when compared to the mass flow rate because the force arch was locally formed in front of the blade. Thus, the 90 percentiles of the

contact force ( $F_{c-90}$ ) was considered to represent the formation tendency of the force arch during the spreading process. The mean  $F_{c-90}$  of GA powder (3.96  $\mu\text{N}$ ) was higher than that of PREP powder (1.79  $\mu\text{N}$ ), indicating frequent force-arch formation in the spreading process. Interestingly, the low mass flow point of the GA powder was comparable to the high  $F_{c-90}$  peaks during the spreading process. This suggests that the particle supply through the gap region was mainly restricted by the formation of a force arch in  $RoI-f$ . Therefore, the powder bed quality of the GA powder can deteriorate owing to the restricted particle supply caused by frequent force arch formation, despite the low residual kinetic energy of the particles.

To clarify the factors determining the powder bed quality in the spreading process, on-site analysis was conducted using four virtual powders:  $P$ -size,  $P$ -shape,  $P$ -friction, and  $P$ -cohesion. The powder beds deposited using the spreading simulation are shown in Fig. 14a–d. The  $\rho_{PB}$  of  $P$ -size (46.5%) was similar to that of the PREP powder (46.6%). The  $\rho_{PB}$  of the PREP powder decreases to 44.8% and 43.8% for  $P$ -shape and  $P$ -friction powders, respectively (Fig. 14b and d). The lowest  $\rho_{PB}$  was obtained in the  $P$ -cohesion powder as to 41.7%, and the surface height variation was further increased. Surface pore analysis was conducted using the image thresholding method to characterize the pore size and number, as shown in Fig. 15a. The surface pore area and number of simulated powder beds are shown in Fig. 15b. The surface pore area of the GA powder was significantly higher than that of the PREP powder, whereas the surface pore number was lower, indicating a large mean pore size. The surface area of  $P$ -size powder was similar to that of the PREP powder, whereas it increased for the  $P$ -shape and  $P$ -friction powders. The surface pore area significantly increased in  $P$ -cohesion powder, whereas the pore number decreased, which was comparable to that of the GA powder. This result indicates that the low packing density of the GA powder is dominantly affected by the cohesive force compared to the presence of nonspherical particles or high interparticle friction.

The contact force and mass flow of the four virtual powders obtained via the on-site analysis are shown in Fig. 16a–d. The mean mass flow of  $P$ -size powder was the highest and the mean  $F_{c-90}$  was the lowest, which

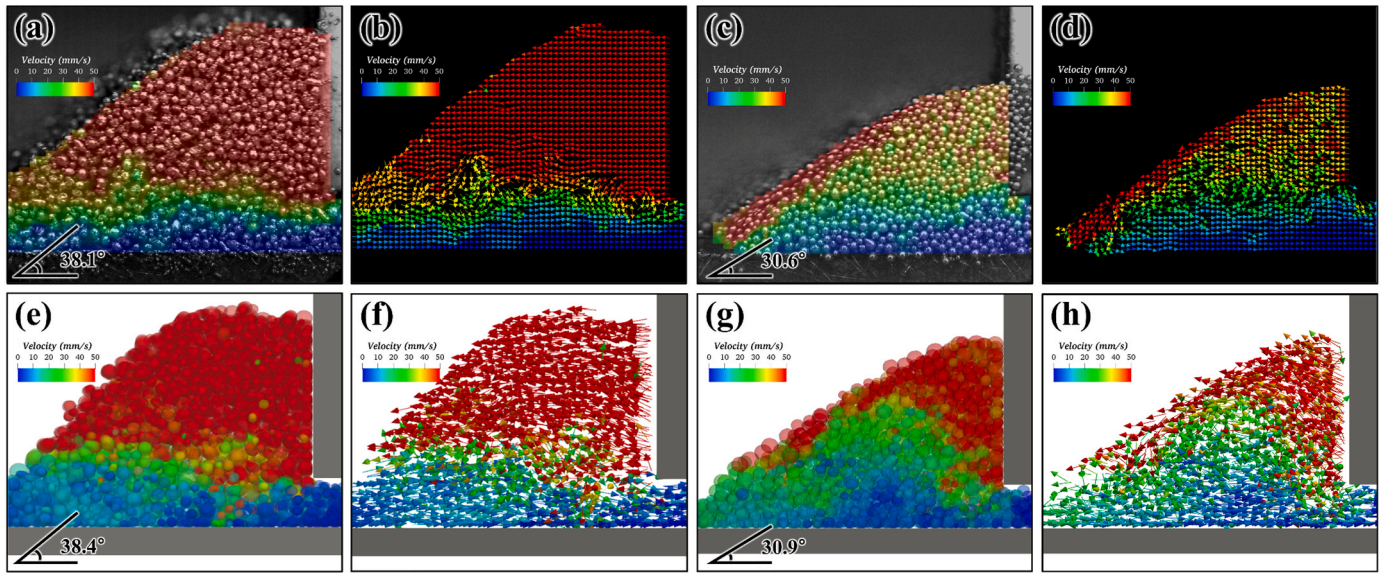


Fig. 10. Particle velocity and displacement via PIV observation and DEM simulation; (a), (b), (c), and (d) experiment, (e), (f), (g), and (h) DEM simulation; (a), (b), (e), and (f) GA powder, (c), (d), (g), and (h) PREP powder.

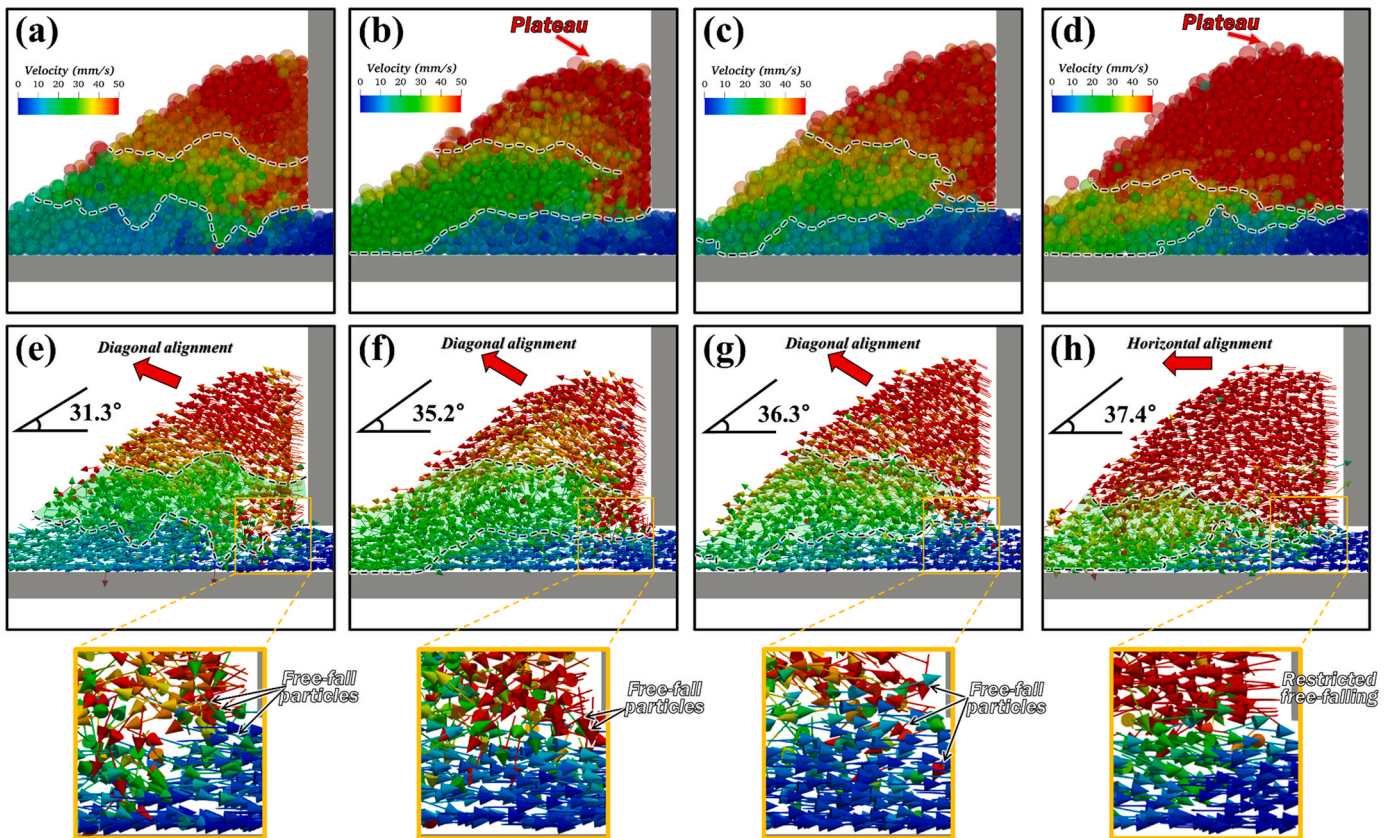
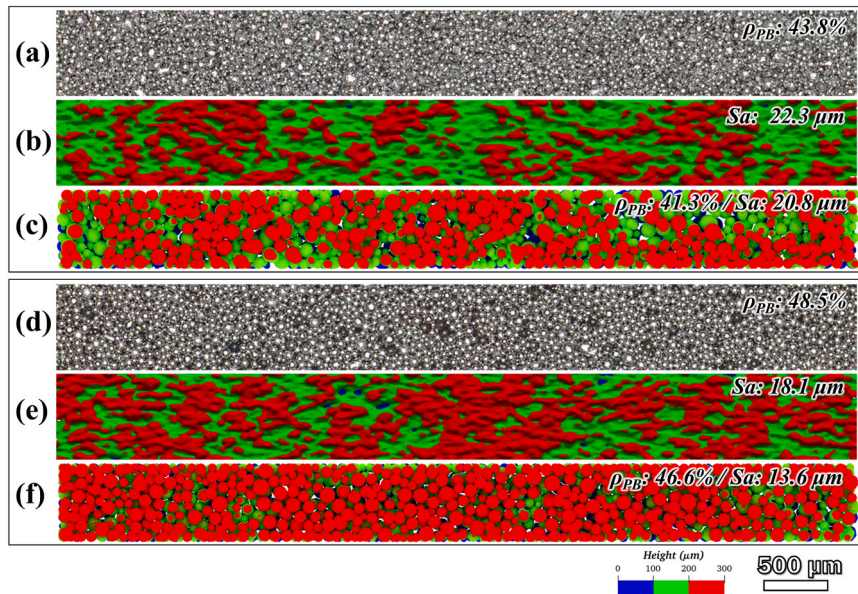


Fig. 11. Snapshot of particle color-coded by velocity in the powder spreading simulation; (a) *P-size*, (b) *P-shape*, (c) *P-friction*, and (d) *P-cohesion* powders; particle displacement color-coded by velocity; (e) *P-size*, (f) *P-shape*, (g) *P-friction*, and (h) *P-cohesion* powders.

matched well with that of the PREP powder. The mean mass flow of *P-shape* powder was  $16.0 \mu\text{g}$ , while the mean  $F_c-90$  was the highest to be  $3.39 \mu\text{N}$ , indicating the frequent formation of force arch. The mean mass flow of *P-friction* powder was lower than that of the *P-shape* powder despite the low mean  $F_c-90$ . The lowest mass flow was obtained in the *P-cohesion* powder, but the mean  $F_c-90$  was examined to be  $3.21 \mu\text{N}$ . This suggests that the trend in  $F_c-90$  does not fully represent the packing

quality of the powder bed during the spreading process.

Snapshots of the powder-spreading simulation, color-coded according to the contact force, are presented in Fig. 17a–l. An insecure force arch was detected in the *P-size* powder, which allowed the supply of dense powder via the gap region during the deposition process (Fig. 17a, e, and i). A strong force arch formed in front of the blade during the spreading process of *P-shape* powder, resulting in a loose powder bed



**Fig. 12.** Snapshot of deposited powder beds in the experiment with height variation; (a), (b) GA powder, (d), (e) PREP powder; simulated powder bed with height variation; (c) GA powder, (f) PREP powder.

(Fig. 17b, f, and j). Chen et al. reported that the addition of elongated particles can suppress the particle supply via the gap region owing to alignment difficulty [40]. Yim et al. demonstrated that the presence of nonspherical particles increases particle interlocking, resulting in the formation of a force arch during the spreading process [28]. Therefore, the particle supply via the gap region could be suppressed in the *P-shape* powder owing to the alignment difficulty of the elongated particles, which causes the frequent formation of force arches. The formation of a strong-force arch was examined in the *P-friction* powder (Fig. 17c, g, and k). Wilson et al. reported that the rough surface of particles can increase the torque required for particle motion, resulting in high interparticle friction [41]. Yim et al. demonstrated that the irregular surface containing fine satellites can cause strong particle interlocking, which activates force arch formation [28]. This result indicates that the force-arch formation can be reinforced by increasing the interparticle friction of the particles, owing to the suppressed particle motion. It is well known that particle flow in a dense powder pile can occur through the temporal void under dynamic conditions (i.e., shaking or vibration), which is also known as granular convection or the Muesli effect [42,43]. Thus, it can be deduced that the particle supply in *P-friction* powder is more limited than that in *P-shape* powder owing to the restricted particle flow through the force arch despite the low mean  $F_c-90$ , as shown in Fig. 16b and c. A strong force arch was observed in the *P-cohesion* powder, and several agglomerates were located near the force arch region (Fig. 17d, h, and l). In the on-site analysis results, the mass flow of *P-cohesion* powder was lower than those of *P-shape* and *P-friction* powders, despite the low mean  $F_c-90$ . Yim et al. reported that the spreadability and packing quality of Ti-48Al-2Cr-2Nb powder were improved by a decrease in the cohesive force via ball milling, despite the irregular shape and high surface roughness [19]. Chen et al. pointed out that the fine particle flow through the gap region is mainly limited by the high cohesive force owing to the formation of agglomerates [25]. This result indicates that the particle flow through the force arch was further suppressed in the *P-cohesion* powder owing to the formation of agglomerates, despite the low  $F_c-90$ . Therefore, the powder bed quality of the GA powder during the spreading process was mainly affected by the cohesive force, which effectively limited the particle supply via the gap region.

### 3.5. Determining factor of cohesive force in powder spreading

As discussed in the previous section, the powder-spreading regime of the PREP powder was significantly altered by the cohesive force, which resulted in a low packing quality of the powder bed. The cohesive force in the powder spreading process can be attributed to several factors, such as capillary, electromagnetic, van der Waals, and electrostatic forces [36]. Cordova et al. reported that the capillary force can strongly increase the cohesive force of metallic powders in a humid environment but becomes predominant at humidity > 80% [44]. Du et al. pointed out that the electromagnetic force can alter the powder spreading and molten pool convection in the LPBF process, but a strong magnetic field > 0.14 T is required to obtain a high Lorentz force [45]. Therefore, the contribution of capillary and static magnetic forces to the cohesive force is negligible under general powder-spreading conditions. The van der Waals force, which is related to the molecular interactions between two spheres, is caused by spontaneous electric polarization in electrically neutral materials. The van der Waals ( $F_V$ ) force between closed particles can be expressed as [46]:

$$F_V = \frac{HR^*}{6d_s^2}, \quad (8)$$

where  $H$  is the Hamaker constant of the material,  $R^*$  is the equivalent radius of  $R^* = R_1R_2/(R_1+R_2)$ , and  $d_s$  is the particle separation distance. The Hamaker constant of the metallic powder can be expressed as [47]:

$$H = \pi^2 C_p \aleph_1 \aleph_2, \quad (9)$$

where  $C_p$  is the potential coefficient in the interaction atom pair, and  $\aleph_1$  and  $\aleph_2$  are the atom number per unit volume in the interface. Therefore, the magnitude of the van der Waals force is highly sensitive to the separation distance between the interfaces, which can result in a cohesive force between particles during the spreading process. It has been reported that a rough powder surface decreases the van der Waals force because of the decreased interaction area [48]. In the SEM image analysis, the surface of the GA particles was rougher than that of the PREP particles owing to the dendritic morphology and surface-attached satellites (Fig. 1a and d). Thus, the van der Waals force between the particles could be reinforced in the PREP powder compared to that in the GA powder. However, in the in situ observation results, the particles in

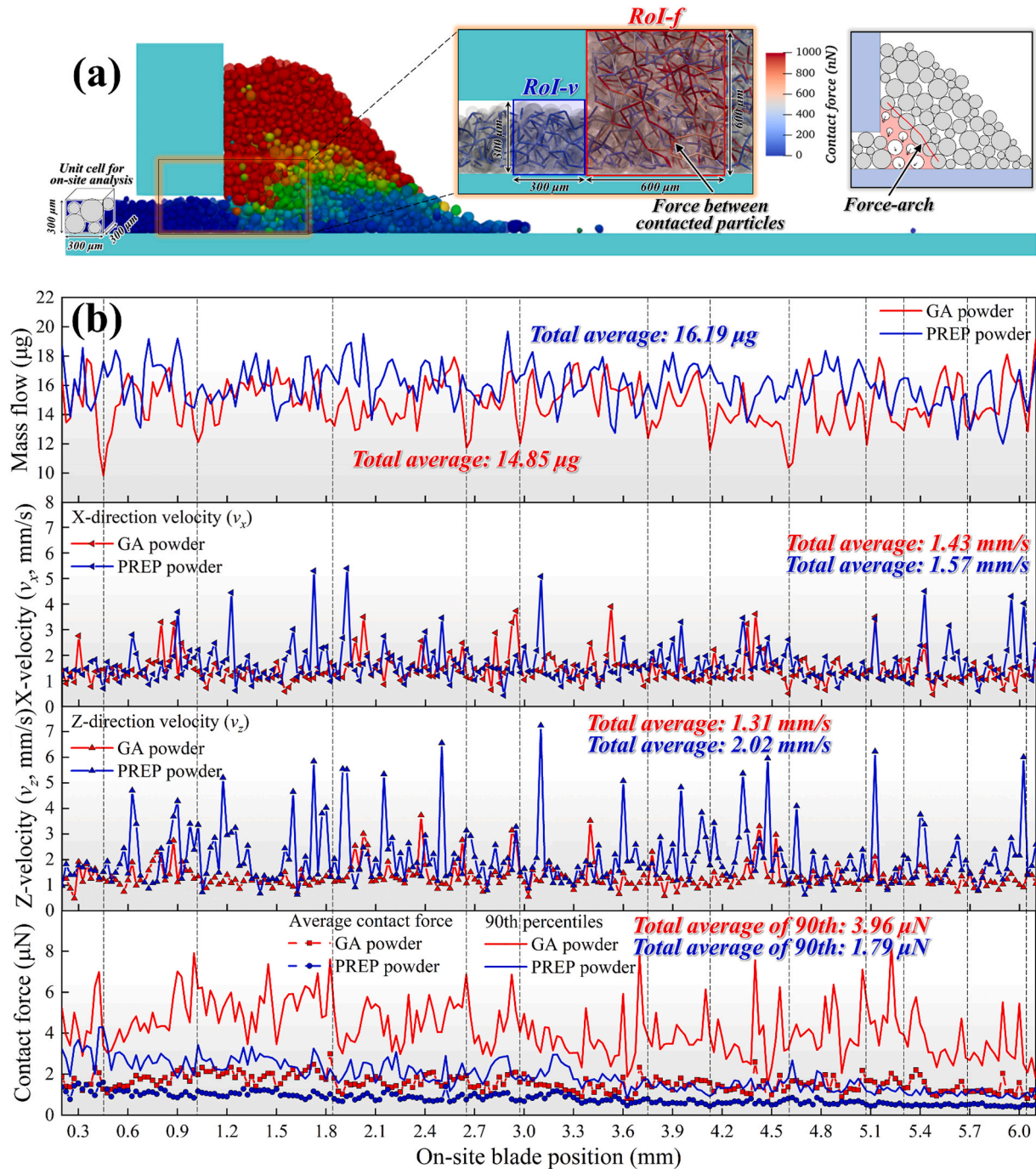


**Fig. 13.** (a) Schematic of powder spreading with on-site analysis boxes, (b) mass flow, velocity components, and contact force of GA and PREP powders in the spreading simulation.

the alignment regime of the PREP powder moved incessantly without forming agglomerates (Fig. 6g–i), while those of the GA powder moved together owing to the severe agglomeration caused by the high cohesive force (Fig. 6a–c). Furthermore, the general acceptance is that the van der Waals force in the metallic powder can exceed gravitational force as decreasing particle size in the powder spreading process, while it was only effective at particle size below 25 μm [23,25,49]. However, the cohesive force in GA powder was dominant in the alignment region regardless of particle size even > 97.6 μm (Fig. 6a–c). This result suggests that the contribution of van der Waals forces could not be significant to the cohesive force of the GA powder during the spreading process. Interestingly, Chiba et al. demonstrated that Inconel718

powder produced via gas atomization does not act as a metallic material but rather as a dielectric material owing to the encapsulated oxide film [50]. More recently, using impedance tests, Yim et al. reported that Ti-48Al-2Cr-2Nb powder produced by gas atomization contained multiple capacitor components because of the presence of multiple oxide films [51,52]. Therefore, it can be deduced that an electrical charge can accumulate on the metallic powder via triboelectric charging under dynamic conditions, causing a cohesive force between the particles [53]. The electrostatic force ( $F_E$ ) originating from the accumulated electric charge on the insulating particles can be expressed as [54].

$$F_E = -\frac{\alpha Q^2}{16\pi\epsilon_0 r^2} + \beta Q E_f - \delta \pi \epsilon_0 r^2 E_f^2, \quad (10)$$

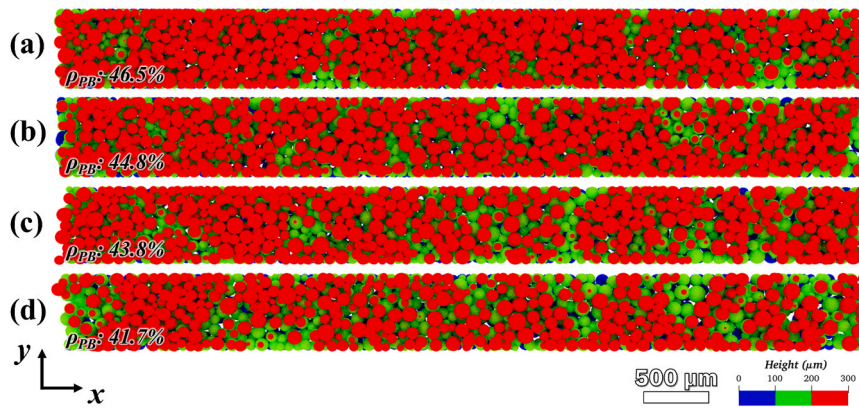


Fig. 14. (a) Deposited powder beds color-coded by height in the spreading simulation; (a) P-size, (b) P-shape, (c) P-friction, (d) P-cohesion powders.

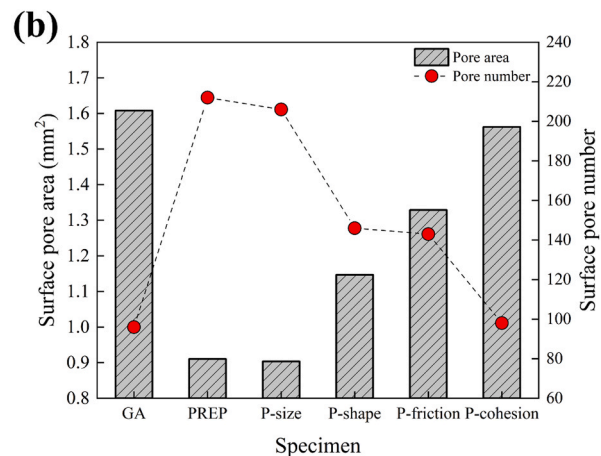
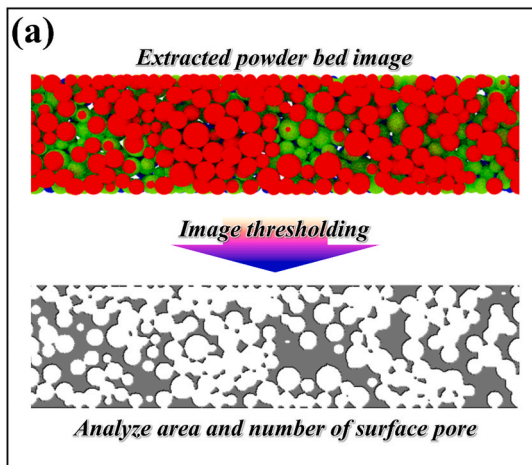


Fig. 15. (a) Schematic of surface pore analysis using the image thresholding method, (b) surface pore area and number in the simulated powder beds.

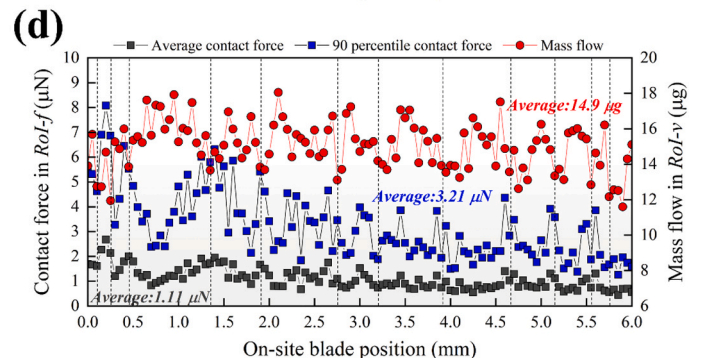
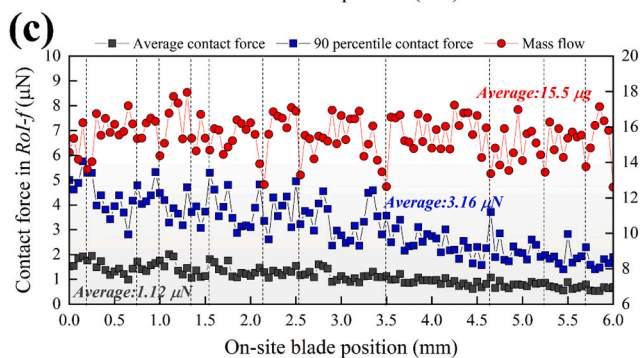
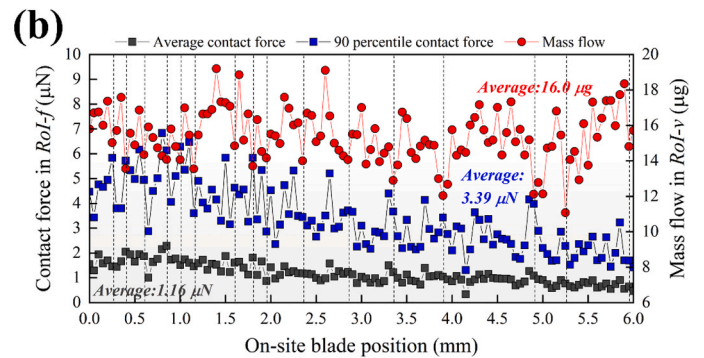
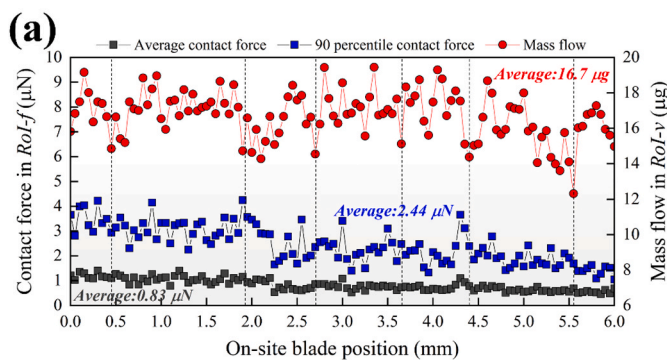


Fig. 16. Contact force and mass flow obtained via on-site analysis; (a) P-size, (b) P-shape, (c) P-friction, and (d) P-cohesion powders.

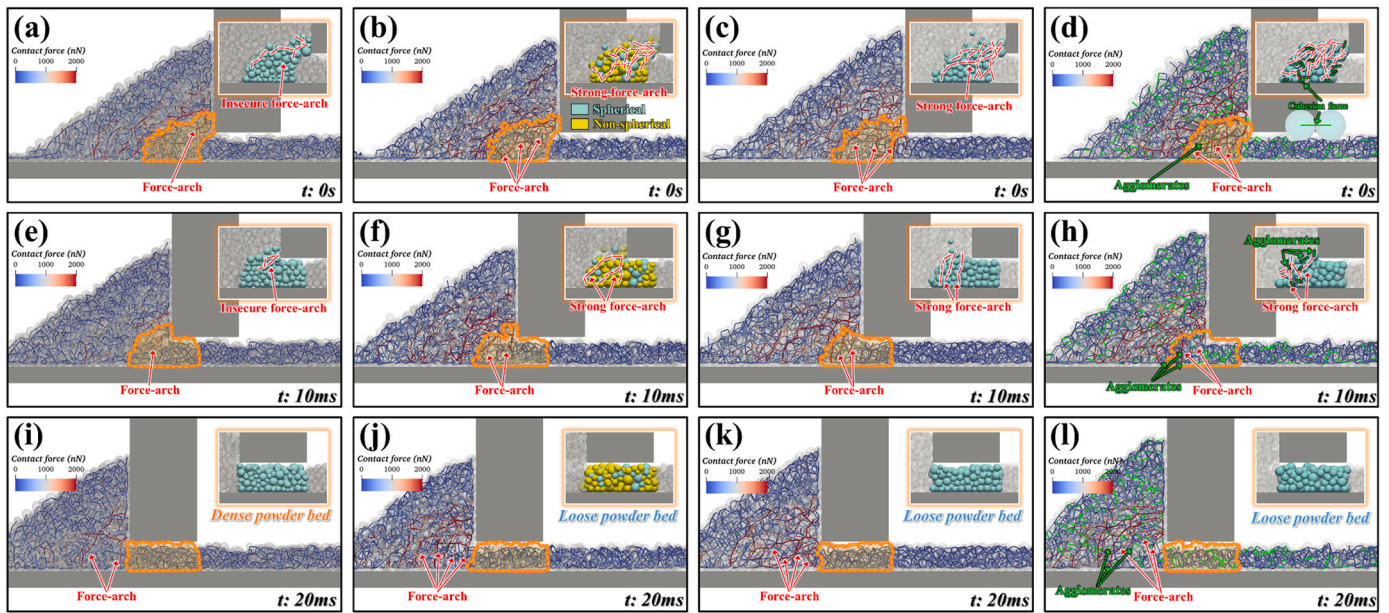


Fig. 17. Snapshots of the powder spreading simulation color-coded by contact force; (a), (e), and (i) *P*-size, (b), (f), and (j) *P*-shape, (c), (g), and (k) *P*-friction, (d), (h), and (l) *P*-cohesion powders; time step of; (a), (b), (c), and (d) 0 s, (e), (f), (g), and (h) 10 ms, (i), (j), (k), and (l) 20 ms.

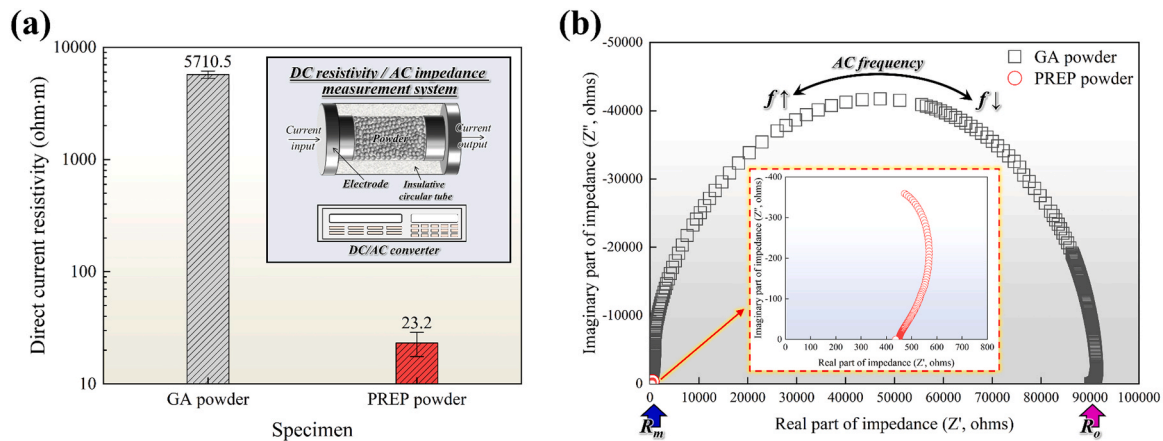


Fig. 18. (a) Direct current resistivity of GA and PREP powders, (b) Nyquist plot of GA and PREP powders obtained by alternative current impedance test.

where  $Q$  is the net charge of the particle,  $E_f$  is the applied electric field,  $\epsilon_0$  is the permittivity of the material,  $r$  is particle radius, and  $\alpha$ ,  $\beta$ , and  $\delta$  are the coefficients related to dielectric constants, surface charge distribution, and particle shape, respectively. Thus, the contribution of the electrostatic force to the cohesive force was significantly affected by the degree of particle charging during the spreading process.

The direct current (DC) resistivities of the GA and PREP powders, measured using the pseudo-four-point probe method, are shown in Fig. 18a. The DC resistivity of GA powder was examined to be 5710.5  $\Omega\cdot\text{m}$ , which is much higher than that of PREP powder about 246 times. Nyquist plots of the GA and PREP powders obtained via alternating-current (AC) impedance tests are shown in Fig. 18b. In the Nyquist plot, the real parts of the impedance in the low-frequency range indicate the ohmic resistance of the metallic inner part ( $R_m$ ), and those in the high-frequency range represent the resistance of the outer oxide film ( $R_o$ ) based on electrical equivalent circuit theory [51]. A semicircle impedance response was obtained in the GA powder depending on the frequency, whereas it disappeared in the PREP powder. The  $R_m$  of GA powder (483.2  $\Omega$ ) was similar to that of PREP powder (472.7  $\Omega$ ), while the  $R_o$  of GA powder (90152.7  $\Omega$ ) was much higher than that of PREP

powder (569.2  $\Omega$ ). This indicates that the capacitor component in the GA powder, which causes electrical charge accumulation, was significantly stronger than that in the PREP powder. The ideal relaxation in a parallel resistor-capacitor circuit can be approximated using Kirchhoff's current law [52]:

$$I_r + I_c = \frac{V}{R} + C \frac{dV}{dt}, \quad (11)$$

$$V(t) = V_i \exp\left(-\frac{t}{RC}\right), \quad (12)$$

where  $I_r$  and  $I_c$  are the current in the resistor and capacitor, respectively,  $C$  is capacitance,  $V_i$  is the initial voltage, and  $\tau$  is the dielectric relaxation time. The charge dissipation time in the resistor-capacitor circuit can be approximated as

$$\tau = \frac{1}{2\pi f_i}, \quad (13)$$

where  $f_i$  denotes the frequency at the inflection point of the impedance data. Further details on the electrical equivalent circuit theory and

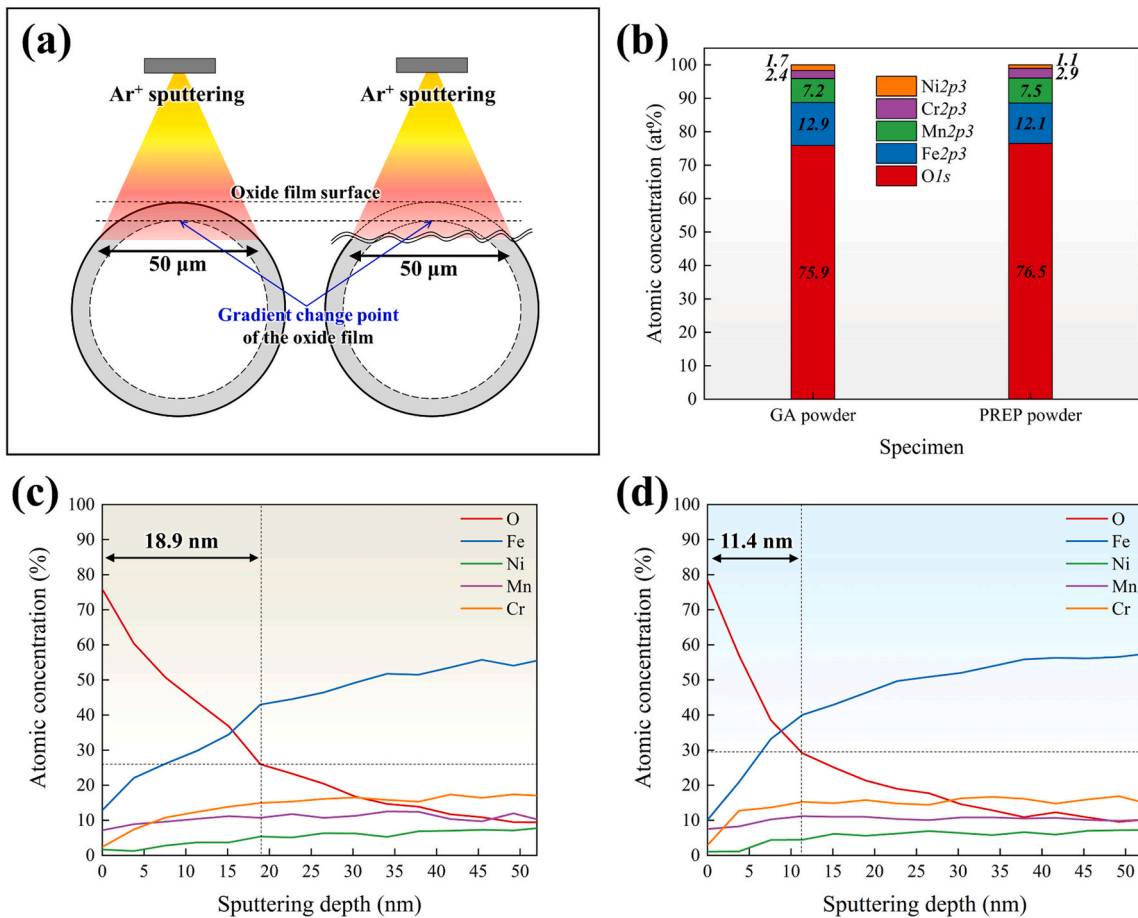


**Fig. 19.** (a) Chemical composition of the outer oxide film in GA and PREP powders by XPS analysis, (b) schematic of depth profiling using the powder specimen; atomic concentration with depth profile; (c) GA powder, (d) PREP powder.

equations can be found in a previous study [55]. The electrical charge in the resistor-capacitor circuit can be expressed as [56]:

$$Q = CV_i(1 - e^{-t/\tau}), \quad (14)$$

where  $t$  is the time after the voltage input. The charge dissipation times of the GA and PREP powders were determined to be  $3.28 \times 10^{-6}$  s and  $0.12 \times 10^{-6}$  s, respectively. This result suggests that triboelectric charging could be further accumulated in the GA powder than in the PREP powder owing to the longer charge relaxation time. Therefore, the high cohesive force of the GA powder can be attributed mainly to the

electrostatic force caused by charge accumulation on the insulating oxide film.

The oxide film compositions of the GA and PREP powders were examined using XPS to determine the reasons for the different capacitive responses. The chemical compositions of the outer oxide films of the GA and PREP powders are shown in Fig. 19a. The oxide film of GA and PREP powders mainly consisted of Fe, Mn, Cr, and Ni oxides, and their atomic concentration was almost similar. The depth profile was obtained using Ar<sup>+</sup> sputtering at an etching rate of 7.27 nm/min, and was calibrated using SiO<sub>2</sub> standards. In the powder sample, the O 1s component was always detectable in the depth profile owing to the encapsulated oxide

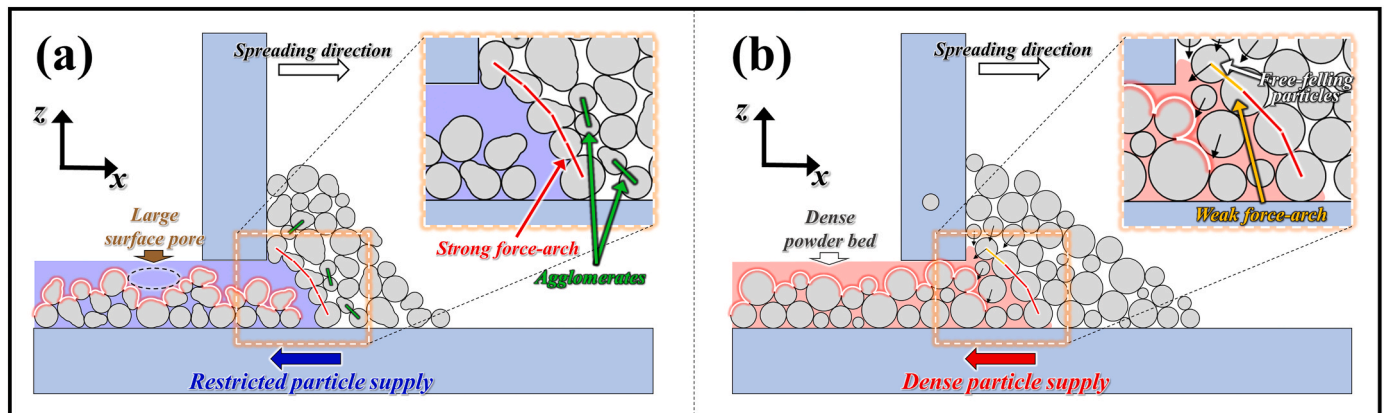


**Fig. 20.** Schematic of the spreading mechanism; (a) GA powder, (b) PREP powder.

film (Fig. 19b). Therefore, the oxide film thickness of the powder can be approximated based on the gradient change in oxygen concentration. The atomic concentrations with depth profiles of the GA and PREP powders are shown in Fig. 19c and d. The oxide film thickness of GA and PREP powders were determined to be 18.9 nm and 11.4 nm, respectively. This result suggests that the strong capacitive response in the GA powder could originate from a thick oxide film, which suppresses charge dissipation through the neighboring particles in contact [57]. Therefore, it can be concluded that the oxide film is a significant factor in determining the powder-spreading behavior and powder bed quality in the PBF-AM process.

Schematics of the spreading mechanism in the GA and PREP powders are presented in Fig. 20a and b. Strong force arches were frequently formed during the spreading of the GA powder by the synergetic effect of elongated particles, high interparticle friction, and cohesive force. The particle supply through the force arch is suppressed by the formation of agglomerates in the GA powder pile. Furthermore, the high cohesive force of the GA powder was mainly attributed to the electrostatic force owing to the thick oxide film, which limited charge dissipation. Thus, a loose powder bed with large surface pores was obtained in the GA powder because of the limited particle supply through the gap region (Fig. 20a). However, an insecure force arch formed in the PREP powder because of the low interparticle friction and cohesive force, which resulted in a dense particle supply via free falling during the spreading process (Fig. 20b). Therefore, a dense powder bed with fine surface pores was obtained in the PREP powder owing to the restricted force arch and particle agglomeration during the spreading process.

#### 4. Conclusion

In this study, the powder-spreading mechanism was investigated using in-situ PIV observations and high-fidelity DEM simulations. The main conclusions drawn from this study are as follows:

1. The powder-spreading mechanism of the GA powder was investigated using PIV. During the spreading process, the kinetic energy supplied to the particles can be depleted via multiple interactions with neighboring particles at a height below the layer thickness. The particle flow regimes in the spreading process can be discriminated based on particle displacement: alignment, rotation, and deposition.
2. The powder-spreading behaviors of the GA and PREP powders were compared using in situ PIV observations. The alignment regime with a high velocity was predominant in the GA powder pile, and the rotation regime with an intermediate velocity prevailed in the PREP powder pile. The particles passing through the gap region in the GA powder were provided along a parabolic direction with a low velocity, whereas those in the PREP powder were supplied by free falling with a high velocity.
3. A high-fidelity discrete element model was developed to clarify the critical factors that determine the spreading mechanism. The high avalanche angle of the GA powder originates from the synergetic effects of the addition of non-spherical particles, high interparticle friction, and high cohesion force. The alignment regime became predominant with increasing cohesive force in the PREP powder. The particle supply in the *P-cohesion* was further suppressed by the formation of a strong force arch and agglomeration during the spreading process. The high cohesive force of the GA powder was attributed to electrostatic forces rather than van der Waals forces.

#### Appendix

##### Simulation parameters validation

The particle flow dynamics in discrete element method (DEM) simulations were determined based on Newtonian second law. Thus, the flow

4. The determining factor of the cohesive force during powder spreading was investigated using DC resistivity and AC impedance tests. The DC resistivity of the GA powder was higher than that of the PREP, and the charge-dissipation time of the GA powder was far higher than that of the PREP powder in the AC impedance test. The strong capacitive response of the GA powder was caused by the thick oxide film, which restricted charge dissipation through the neighboring particles in contact.

In conclusion, it was demonstrated that the oxide film is a critical factor in controlling the powder-spreading behavior and powder bed quality in the PBF-AM process.

#### CRediT authorship contribution statement

**Koki Minowa:** Investigation. **Jiayu Sun:** Writing – review & editing, Investigation. **Kenta Aoyagi:** Writing – review & editing, Resources. **Hao Wang:** Writing – review & editing. **Kenta Yamanaka:** Writing – review & editing, Resources. **Akihiko Chiba:** Writing – review & editing, Supervision, Project administration, Funding acquisition, Conceptualization. **Seungkyun Yim:** Writing – original draft, Visualization, Validation, Software, Methodology, Investigation, Formal analysis, Conceptualization.

#### Declaration of Competing Interest

The authors declare the following financial interests/personal relationships which may be considered as potential competing interests: One of the authors of this article are a part of the Editorial Board of the journal. To avoid a potential conflict of interest, the re-sponsibility for the editorial and peer-review process of this article was handled by a different editor. Furthermore, the authors of this article were removed from the peer review process and had no, and will not have, any access to confidential information related to the editorial process of this article.

#### Data Availability

The authors are unable or have chosen not to specify which data has been used.

#### Acknowledgements

This study was partially supported by JSPS KAKENHI [grant number 18H05455]. This research was partially supported by Materials Integration for Revolutionary Design System of Structural Materials of the Cross-Ministerial Strategic Innovation Promotion Program (SIP) of Japan Science and Technology (JST). This study was supported in part by the Technology Research Association for Future Additive Manufacturing (TRAFAM). This work was partially supported by the Innovative Structural Materials Association (ISMA) commissioned by the New Energy and Industrial Technology Development Organization (NEDO). This work was also partially supported by the JST Moonshot R&D-Self-evolving AI Robot System for Lunar Exploration and Human Outpost Construction Program [grant number JPMJMS223B]. The authors also thank Sato Tsukasa, Institute for Materials Research, Tohoku University, for developing the powder-spreading devices.

regimes of the powder are significantly affected by damping parameters, such as the restitution coefficient, sliding friction, rolling friction, and cohesion force. In this study, the damping coefficients in the DEM simulation were calibrated under static and rotating conditions, because the powder pile in the spreading process contained static (alignment) and rotation regimes. A flowability experiment under static conditions was conducted using a Hall flowmeter (JIS-Z2502, Tsutsui Scientific Instruments Co., Ltd., Japan) following the ASTM B213 standard. The powder (50 g) was inserted into the flow hole, and the flow time was checked using laser detectors. The mass flow rate of GA and PREP powders were determined to be 3.32 g/s and 3.81 g/s, respectively. The particle flow was stopped and the powder pile image was captured in the upper and front directions using a digital single-lens reflex camera at a fixed position. The avalanche angle of the deposited powder pile was analyzed using the edge-tracing linear regression method. A Hall-flow simulation was developed to calibrate the damping factors under static conditions. The simulation scale was reduced to 1/40 considering the computational cost. The powder piles deposited in the experiment and simulation are presented in Fig. A1a–d. The area factor ( $f_A$ ) of the deposited powder was defined as follows:

$$f_A = \frac{A_p}{A_i} \times 100, \quad (1)$$

where  $A_p$  is the area occupied by the deposited powder, and  $A_i$  is the area of the imaginary octagonal plate. In the experimental results, the  $f_A$  of GA powder was lower than that of the PREP powder, which agrees well with the results of the DEM simulation.

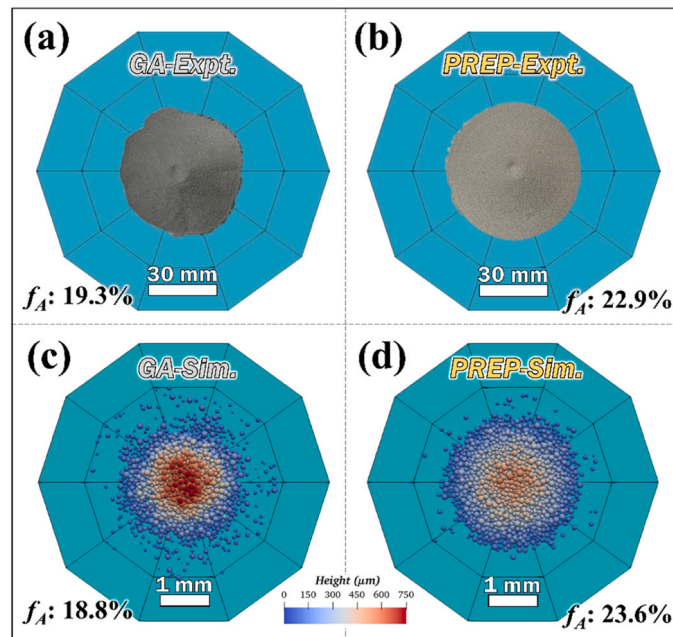


**Fig. A1.** Top view of deposited powder piles via the Hall flowmeter test; (a), (b) experimental result, (c), (d) DEM simulation result; (a), (c) GA SUS304 powder, (b), (d) PREP SUS304 powder.

The avalanche angles of the deposited powder piles in the experiment and simulation are described in Fig. A2a and b. The avalanche angle of the GA powder was higher than that of the PREP powder, and the trend matched well with the simulation results. Thus, the damping parameter under static conditions was calibrated well by fitting the  $f_A$  and avalanche angles obtained via the Hall flowmeter test. By contrast, surface wrinkles were observed on the GA powder pile, whereas they disappeared on the PREP powder pile. This result suggests that the cohesive force between the particles may be much higher in the GA powder than in the PREP powder.

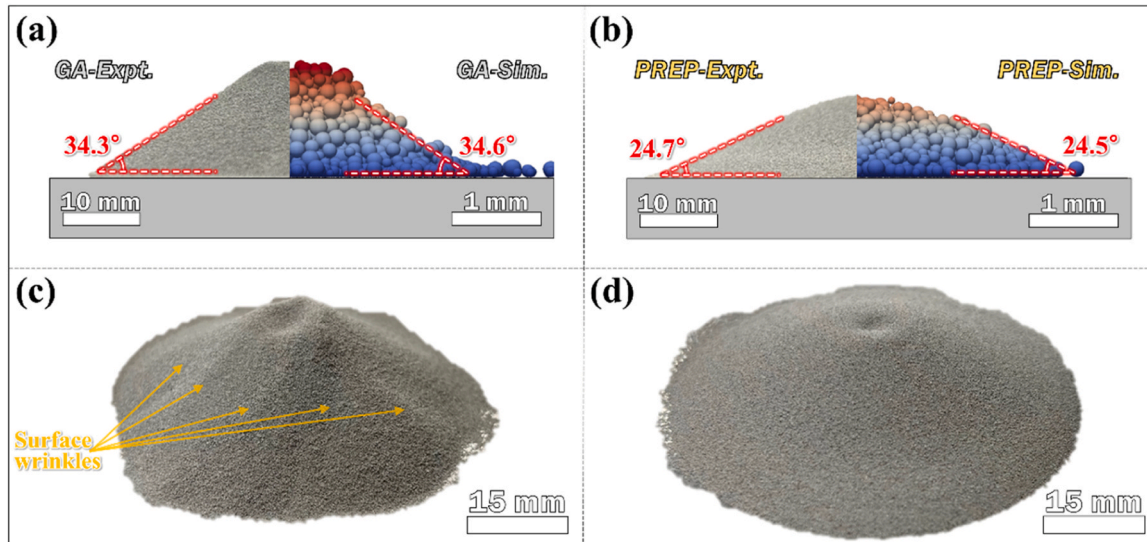


**Fig. A2.** Front view of deposited powder piles obtained via the experiment and simulation; (a) GA SUS304 powder, (b) PREP SUS304 powder; The tilted view of deposited powder pile in the experiment; (c) GA SUS304 powder, (d) PREP SUS304 powder.

A rotating-drum test was performed to calibrate the damping parameters of the simulation under dynamic conditions. The optical rotating drum was filled with 30 vol% by powder and then rotated clockwise at an angular velocity of 10 rpm. The particle flow regime under rotation was recorded using the digital single-lens reflex camera at an acquisition rate of 60 images/s. A rotating-drum simulation was developed to calibrate the damping coefficient under dynamic conditions. The simulation scale was reduced to 1/20 to reduce the computational time. Snapshots of the rotating-drum test in the experiment and simulation are presented in Fig. A3a–d. The avalanche angle of the GA powder was higher than that of the PREP powder, which agrees well with the simulation trend despite different system scales of experiment and simulation. Thus, we assumed that the scale conversion effect in DEM simulation can be negligible under static and dynamic conditions. Therefore, the damping parameters for the GA and PREP powders were accurately calibrated by comparing the avalanche angles under static and dynamic conditions.

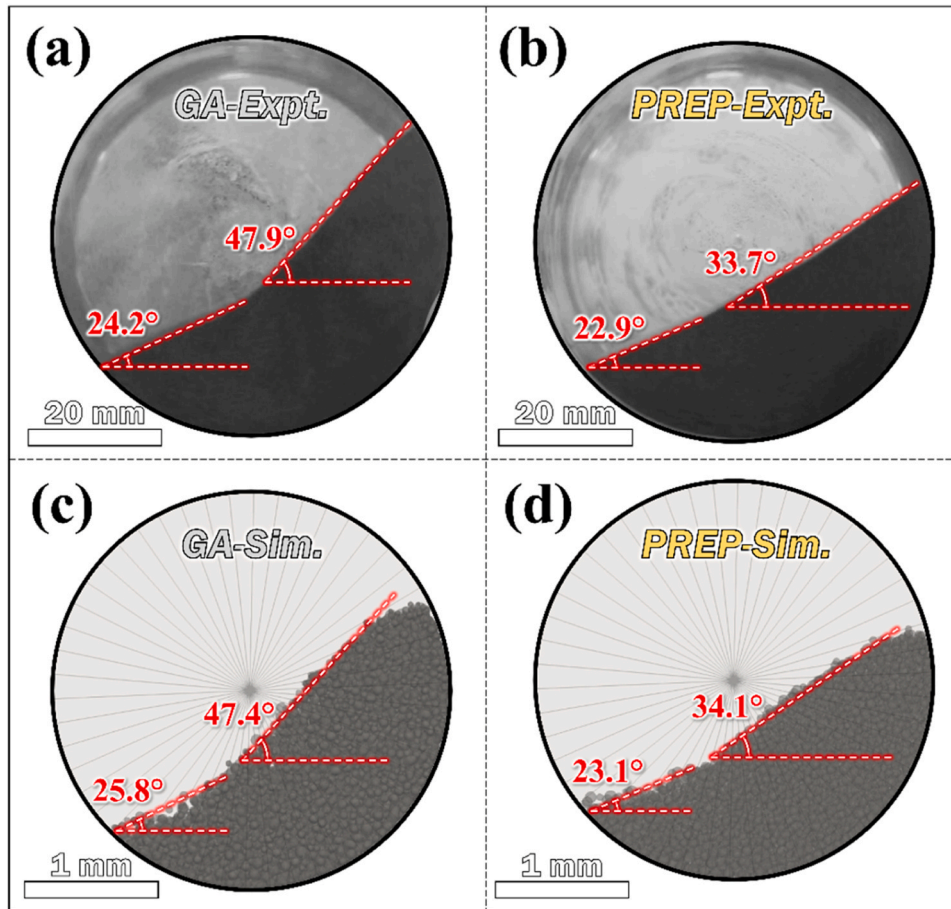


**Fig. A3.** Snapshots of the rotating drum test with an angular velocity of 10 rpm; (a), (b) experimental result, (c), (d) DEM simulation result; (a), (c) GA SUS304 powder, (b), (d) PREP SUS304 powder.

The snapshot of the PREP spreading model at the side and front view is presented in Fig. A4. The particle flow regimes in the spreading simulation were examined at the outer and inner regions to prove the validity of in-situ observations using the flexible glass (Fig. A4a2). The particle velocity distribution at the outer and inner regions was similar (Fig. A4b1 and c1), and its displacement was aligned with the diagonal direction, which was well matched with the experimental result (Fig. A4b2 and c2). The modified displacement at outer and inner regions was slightly different, but the dominant rotational regimes were observed (Fig. A4b3 and c3). This result indicates that the different physical properties of optical glass are a minor factor in determining the particle flow regimes in the spreading process. Therefore, it was demonstrated that in situ observation via optical glass can represent the whole powder spreading regimes in the powder spreading process.

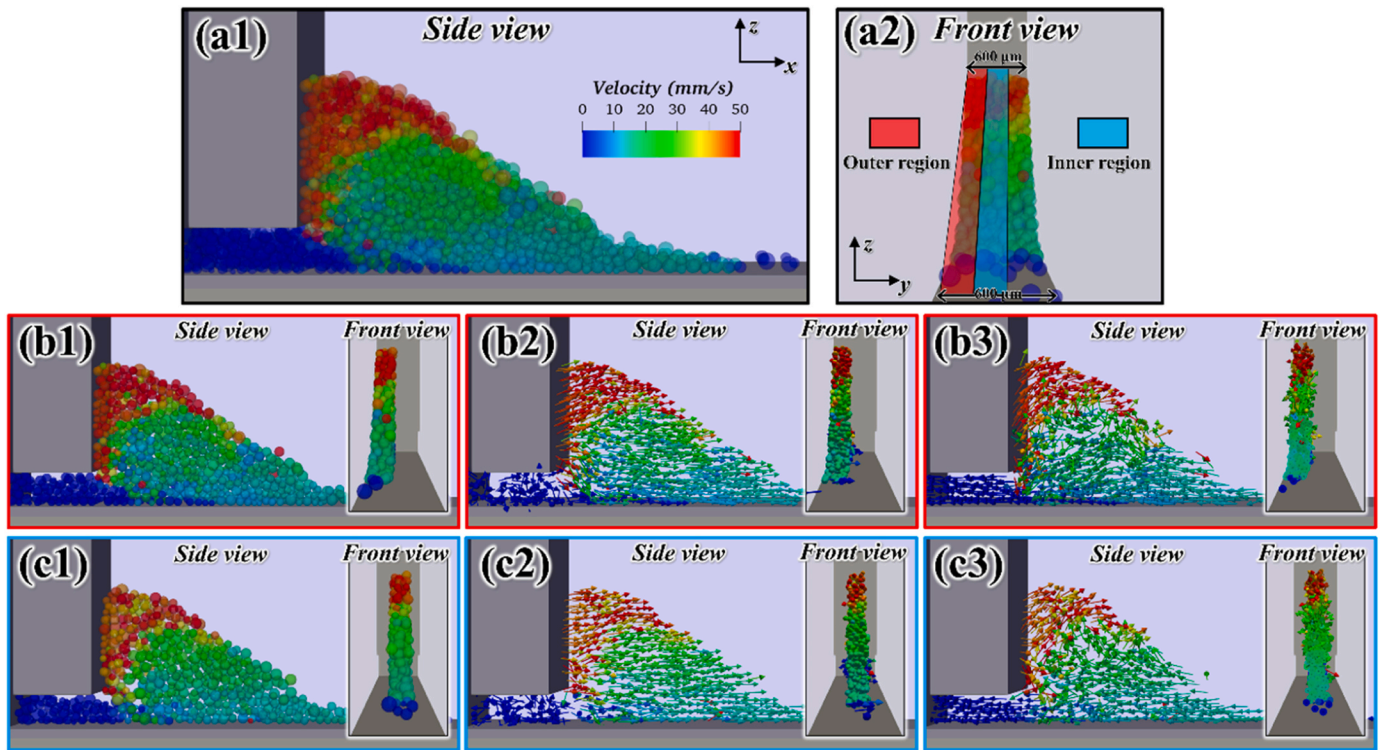


**Fig. A4.** Snapshots of the PREP spreading simulation; (a1), (a2) side and front view of total region, (b1), (b2), (b3) side and front view of outer region, (c1), (c2), (c3) side and front view of inner region; (a1), (b1), (c1) particles color-coded velocity, (b2), (c2) displacement color-coded by velocity, (b3), (c3) modified displacement color-coded by velocity.

## References

- [1] T.D. Ngo, A. Kashani, G. Imbalzano, K.T.Q. Nguyen, D. Hui, Additive manufacturing (3D printing): a review of materials, methods, applications and challenges, *Compos. Part B Eng.* 143 (2018) 172–196, <https://doi.org/10.1016/j.compositesb.2018.02.012>.
- [2] H.R. Kotadia, G. Gibbons, A. Das, P.D. Howes, A review of Laser Powder Bed Fusion Additive Manufacturing of aluminium alloys: microstructure and properties, *Addit. Manuf.* 46 (2021), 102155, <https://doi.org/10.1016/j.addma.2021.102155>.
- [3] M. Galati, L. Iuliano, A literature review of powder-based electron beam melting focusing on numerical simulations, *Addit. Manuf.* 19 (2018) 1–20, <https://doi.org/10.1016/j.addma.2017.11.001>.
- [4] S. Sun, M. Brandt, M. Easton, 2 - Powder bed fusion processes: an overview, in: M. Brandt (Ed.), *Laser Addit. Manuf.*, Woodhead Publishing, 2017, pp. 55–77, <https://doi.org/10.1016/B978-0-08-100433-3.00002-6>.
- [5] Y. Lei, K. Aoyagi, Y. Cui, D.S. Kang, K. Kuwabara, K. Aota, A. Chiba, Process optimization and mechanical property investigation of non-weldable superalloy Alloy713ELC manufactured with selective electron beam melting, *Mater. Sci. Eng. A* 787 (2020), 139485, <https://doi.org/10.1016/j.msea.2020.139485>.
- [6] C.L.A. Leung, R. Tosi, E. Muzangaza, S. Nonni, P.J. Withers, P.D. Lee, Effect of preheating on the thermal, microstructural and mechanical properties of selective electron beam melted Ti-6Al-4V components, *Mater. Des.* 174 (2019), 107792, <https://doi.org/10.1016/j.matdes.2019.107792>.
- [7] S.F. Li, K. Geng, R.D.K. Misra, J.Y. Cui, D. Ye, Y. Liu, Y.F. Yang, Commercial scale uniform powder coating for metal additive manufacturing, *Jom* 72 (2020) 4639–4647, <https://doi.org/10.1007/s11837-020-04386-z>.
- [8] P. Fernandez-Zelaia, M.M. Kirka, A.M. Rossy, Y. Lee, S.N. Dreypondt, Nickel-based superalloy single crystals fabricated via electron beam melting, *Acta Mater.* 216 (2021), 117133, <https://doi.org/10.1016/j.actamat.2021.117133>.
- [9] X. Wang, J.A. Muñoz-Lerma, O. Sanchez-Mata, M. Attarian Shandiz, N. Brodusch, R. Gauvin, M. Brochu, Characterization of single crystalline austenitic stainless steel thin struts processed by laser powder bed fusion, *Scr. Mater.* 163 (2019) 51–56, <https://doi.org/10.1016/j.scriptamat.2018.12.032>.
- [10] Y. Lei, K. Aoyagi, A. Chiba, A method to manipulate non-steady-state columnar-to-equiaxed transition in powder bed fusion additive manufacturing using an electron beam, *Acta Mater.* 227 (2022), 117717, <https://doi.org/10.1016/j.actamat.2022.117717>.
- [11] J.A. Koepf, M.R. Gotterbarm, M. Markl, C. Körner, 3D multi-layer grain structure simulation of powder bed fusion additive manufacturing, *Acta Mater.* 152 (2018) 119–126, <https://doi.org/10.1016/j.actamat.2018.04.030>.
- [12] K. Aoyagi, H. Wang, H. Sudo, A. Chiba, Simple method to construct process maps for additive manufacturing using a support vector machine, *Addit. Manuf.* 27 (2019) 353–362, <https://doi.org/10.1016/j.addma.2019.03.013>.
- [13] Y. Gui, K. Aoyagi, H. Bian, A. Chiba, Detection, classification and prediction of internal defects from surface morphology data of metal parts fabricated by powder bed fusion type additive manufacturing using an electron beam, *Addit. Manuf.* 54 (2022), 102736, <https://doi.org/10.1016/j.addma.2022.102736>.
- [14] A.M. Rausch, V.E. Küng, C. Pobel, M. Markl, C. Körner, Predictive simulation of process windows for powder bed fusion additive manufacturing: influence of the powder bulk density, *Materials* 10 (2017), <https://doi.org/10.3390/ma10101117>.
- [15] Y. Zhao, K. Aoyagi, Y. Daino, K. Yamanaka, A. Chiba, Significance of powder feedstock characteristics in defect suppression of additively manufactured Inconel 718, *Addit. Manuf.* 34 (2020), 101277, <https://doi.org/10.1016/j.addma.2020.101277>.
- [16] Z. Snow, R. Martukanitz, S. Joshi, On the development of powder spreadability metrics and feedstock requirements for powder bed fusion additive manufacturing, *Addit. Manuf.* 28 (2019) 78–86, <https://doi.org/10.1016/j.addma.2019.04.017>.
- [17] W. Nan, Y. Gu, Experimental investigation on the spreadability of cohesive and frictional powder, *Adv. Powder Technol.* 33 (2022), 103466, <https://doi.org/10.1016/j.apt.2022.103466>.
- [18] A. Mussatto, R. Groarke, A. O'Neill, M.A. Obeidi, Y. Delaure, D. Brabazon, Influences of powder morphology and spreading parameters on the powder bed topography uniformity in powder bed fusion metal additive manufacturing, *Addit. Manuf.* 38 (2021), 101807, <https://doi.org/10.1016/j.addma.2020.101807>.
- [19] S. Yim, K. Aoyagi, H. Bian, Y. Cui, A. Chiba, Factors determining the flowability and spreading quality of gas-atomized Ti-48Al-2Cr-2Nb powders in powder bed fusion additive manufacturing, *Powder Technol.* 412 (2022), 117996, <https://doi.org/10.1016/j.powtec.2022.117996>.
- [20] Y. Lee, A.K. Gurnon, D. Bodner, S. Simunovic, Effect of particle spreading dynamics on powder bed quality in metal additive manufacturing, *Integr. Mater. Manuf. Innov.* 9 (2020) 410–422, <https://doi.org/10.1007/s40192-020-00193-1>.
- [21] L.I. Escano, N.D. Parab, L. Xiong, Q. Guo, C. Zhao, K. Fezzaa, W. Everhart, T. Sun, L. Chen, Revealing particle-scale powder spreading dynamics in powder-bed-based additive manufacturing process by high-speed x-ray imaging, *Sci. Rep.* 8 (2018) 1–11, <https://doi.org/10.1038/s41598-018-33376-0>.
- [22] L.I. Escano, N.D. Parab, Q. Guo, M. Qu, K. Fezzaa, W. Everhart, T. Sun, L. Chen, An instrument for in situ characterization of powder spreading dynamics in powder-bed-based additive manufacturing processes, *Rev. Sci. Instrum.* 93 (2022), <https://doi.org/10.1063/5.0076235>.
- [23] C. Meier, R. Weissbach, J. Weinberg, W.A. Wall, A.J. Hart, Critical influences of particle size and adhesion on the powder layer uniformity in metal additive

- manufacturing, *J. Mater. Process. Technol.* 266 (2019) 484–501, <https://doi.org/10.1016/j.jmatprotec.2018.10.037>.
- [24] Y. He, A. Hassanpour, A.E. Bayly, Combined effect of particle size and surface cohesiveness on powder spreadability for additive manufacturing, *Powder Technol.* 392 (2021) 191–203, <https://doi.org/10.1016/j.powtec.2021.06.046>.
- [25] H. Chen, Q. Wei, Y. Zhang, F. Chen, Y. Shi, W. Yan, Powder-spreading mechanisms in powder-bed-based additive manufacturing: experiments and computational modeling, *Acta Mater.* 179 (2019) 158–171, <https://doi.org/10.1016/j.actamat.2019.08.030>.
- [26] W. Nan, M. Pasha, M. Ghadiri, Numerical simulation of particle flow and segregation during roller spreading process in additive manufacturing, *Powder Technol.* 364 (2020) 811–821, <https://doi.org/10.1016/j.powtec.2019.12.023>.
- [27] S. Yim, H. Bian, K. Aoyagi, K. Yamanaka, A. Chiba, Spreading behavior of Ti–48Al–2Cr–2Nb powders in powder bed fusion additive manufacturing process: experimental and discrete element method study, *Addit. Manuf.* 49 (2022), 102489, <https://doi.org/10.1016/j.addma.2021.102489>.
- [28] S. Yim, H. Bian, K. Aoyagi, K. Yamanaka, A. Chiba, Effect of powder morphology on flowability and spreading behavior in powder bed fusion additive manufacturing process: a particle-scale modeling study, *Addit. Manuf.* 72 (2023), 103612, <https://doi.org/10.1016/j.addma.2023.103612>.
- [29] Y.S. Lee, P. Nandwana, W. Zhang, Dynamic simulation of powder packing structure for powder bed additive manufacturing, *Int. J. Adv. Manuf. Technol.* 96 (2018) 1507–1520, <https://doi.org/10.1007/s00170-018-1697-3>.
- [30] J. Végh, The Shirley background revised, *J. Electron Spectros. Relat. Phenom.* 151 (2006) 159–164, <https://doi.org/10.1016/j.elspec.2005.12.002>.
- [31] H. Chen, T. Cheng, Z. Li, Q. Wei, W. Yan, Is high-speed powder spreading really unfavourable for the part quality of laser powder bed fusion additive manufacturing, *Acta Mater.* 231 (2022), 117901, <https://doi.org/10.1016/j.actamat.2022.117901>.
- [32] R.D. Keane, R.J. Adrian, Theory of cross-correlation analysis of PIV images, *Appl. Sci. Res.* 49 (1992) 191–215, <https://doi.org/10.1007/BF00384623>.
- [33] W. Thielicke, R. Sonntag, Particle image velocimetry for MATLAB: accuracy and enhanced algorithms in PIVlab, *J. Open Res. Softw.* 9 (2021) 1–14, <https://doi.org/10.5334/JORS.334>.
- [34] V. Smilauer, E. Catalano, B. Chareyre, *Yade Documentation*, second ed., The Yade Project, 2015 <https://doi.org/10.5281/zenodo.34073>.
- [35] P.A. Cundall, O.D.L. Strack, A discrete numerical model for granular assemblies, *Géotechnique* 29 (1979) 47–65, <https://doi.org/10.1680/geot.1979.29.1.47>.
- [36] J. Visser, Van der Waals and other cohesive forces affecting powder fluidization, *Powder Technol.* 58 (1989) 1–10, [https://doi.org/10.1016/0032-5910\(89\)80001-4](https://doi.org/10.1016/0032-5910(89)80001-4).
- [37] D. Violato, P. Moore, F. Scarano, Lagrangian and Eulerian pressure field evaluation of rod-airfoil flow from time-resolved tomographic PIV, *Exp. Fluids* 50 (2011) 1057–1070, <https://doi.org/10.1007/s00348-010-1011-0>.
- [38] M.J. Sholl, Savaş, A fast lagrangian piv method for study of general high-gradient flows, 35th Aerosp. Sci. Meet. Exhib. (1997). <https://doi.org/10.2514/6.1997-493>.
- [39] H.R. Norouzi, R. Zarghami, N. Mostoufi, Insights into the granular flow in rotating drums, *Chem. Eng. Res. Des.* 102 (2015) 12–25, <https://doi.org/10.1016/j.cherd.2015.06.010>.
- [40] H. Chen, T. Cheng, Q. Wei, W. Yan, Dynamics of short fiber/polymer composite particles in paving process of additive manufacturing, *Addit. Manuf.* 47 (2021), 102246, <https://doi.org/10.1016/j.addma.2021.102246>.
- [41] R. Wilson, D. Dini, B. Van Wachem, The influence of surface roughness and adhesion on particle rolling, *Powder Technol.* 312 (2017) 321–333, <https://doi.org/10.1016/j.powtec.2017.01.080>.
- [42] W. SOPPE, Computer simulation of random packing of hard spheres, *Powder Technol.* 62 (1990) 189–196, [https://doi.org/10.1016/0032-5910\(90\)80083-B](https://doi.org/10.1016/0032-5910(90)80083-B).
- [43] C. Zeilstra, J.G. Collignon, M.A. van der Hoef, N.G. Deen, J.A.M. Kuipers, Experimental and numerical study of wall-induced granular convection, *Powder Technol.* 184 (2008) 166–176, <https://doi.org/10.1016/j.powtec.2007.11.037>.
- [44] L. Cordova, T. Bor, M. de Smit, M. Campos, T. Tinga, Measuring the spreadability of pre-treated and moisturized powders for laser powder bed fusion, *Addit. Manuf.* 32 (2020), 101082, <https://doi.org/10.1016/j.addma.2020.101082>.
- [45] D. Du, L. Wang, A. Dong, W. Yan, G. Zhu, B. Sun, Promoting the densification and grain refinement with assistance of static magnetic field in laser powder bed fusion, *Int. J. Mach. Tools Manuf.* 183 (2022), 103965, <https://doi.org/10.1016/j.ijmactools.2022.103965>.
- [46] H.C. Hamaker, The London-van der Waals attraction between spherical particles, *Physica* 4 (1937) 1058–1072, [https://doi.org/10.1016/S0031-8914\(37\)80203-7](https://doi.org/10.1016/S0031-8914(37)80203-7).
- [47] S. Lee, W.M. Sigmund, AFM study of repulsive van der Waals forces between Teflon AF™ thin film and silica or alumina, 204 (2002) 43–50.
- [48] F.W. Delrio, M.P. De Boer, J.A. Knapp, E.D. Reedy, P.J. Clews, M.L. Dunn, The role of van der Waals forces in adhesion of micromachined surfaces, *Nat. Mater.* 4 (2005) 629–634, <https://doi.org/10.1038/nmat1431>.
- [49] C. Meier, R. Weissbach, J. Weinberg, W.A. Wall, A. John Hart, Modeling and characterization of cohesion in fine metal powders with a focus on additive manufacturing process simulations, *Powder Technol.* 343 (2019) 855–866, <https://doi.org/10.1016/j.powtec.2018.11.072>.
- [50] A. Chiba, Y. Daino, K. Aoyagi, K. Yamanaka, Smoke suppression in electron beam melting of inconel 718 alloy powder based on insulator – metal transition of surface, *Mater* 14 (2021), <https://doi.org/10.3390/ma14164662>.
- [51] S. Yim, H. Bian, K. Aoyagi, K. Yanagihara, S. ichi Kitamura, H. Manabe, Y. Daino, Y. Hayasaka, K. Yamanaka, A. Chiba, Ball-milling treatment of gas-atomized Ti–48Al–2Cr–2Nb powder and its effect on preventing smoking during electron beam powder bed fusion building process, *Addit. Manuf.* 51 (2022), 102634, <https://doi.org/10.1016/j.addma.2022.102634>.
- [52] S. Yim, K. Aoyagi, K. Yanagihara, H. Bian, A. Chiba, Effect of mechanical ball milling on the electrical and powder bed properties of gas-atomized Ti–48Al–2Cr–2Nb and elucidation of the smoke mechanism in the powder bed fusion electron beam melting process, *J. Mater. Sci. Technol.* 137 (2022) 36–55, <https://doi.org/10.1016/j.jmst.2022.07.024>.
- [53] S. Matsusaka, H. Maruyama, T. Matsuyama, M. Ghadiri, Triboelectric charging of powders: a review, *Chem. Eng. Sci.* 65 (2010) 5781–5807, <https://doi.org/10.1016/j.ces.2010.07.005>.
- [54] J.Q. Feng, D.A. Hays, A finite-element analysis of the electrostatic force on a uniformly charged dielectric sphere resting on a dielectric-coated electrode in a detaching electric field, *IEEE Trans. Ind. Appl.* 34 (1998) 84–91, <https://doi.org/10.1109/28.658725>.
- [55] E.Von Hauff, Impedance spectroscopy for emerging photovoltaics, *J. Phys. Chem. C* 123 (2019) 11329–11346, <https://doi.org/10.1021/acs.jpcc.9b00892>.
- [56] Z.C. Cordero, H.M. Meyer, P. Nandwana, R.R. Dehoff, Powder bed charging during electron-beam additive manufacturing, *Acta Mater.* 124 (2017) 437–445, <https://doi.org/10.1016/j.actamat.2016.11.012>.
- [57] J. Li, Y. Li, Z. Wang, H. Bian, Y. Hou, F. Wang, G. Xu, B. Liu, Y. Liu, Ultrahigh oxidation resistance and high electrical conductivity in copper-silver powder, *Sci. Rep.* 6 (2016) 1–10, <https://doi.org/10.1038/srep39650>.